Experimental Study of Aeropropulsive Interactions for Electric Ducted Fans on a Wing

Rose Weinstein*, Vincent A. Spada†, and Benjamin M. Simmons‡
NASA Langley Research Center, Hampton, Virginia, 23681

The Adaptable Distributed Electric Propulsion Testbed (ADEPT) Wing was tested in the NASA Langley 12-Foot Low-Speed Tunnel to investigate electric propulsion technologies for commercial transport aircraft. The purpose of the test was to study the aeropropulsive effects across angle of attack and fan speed variations for several propulsor placements and array sizes, and to investigate how distributed electric propulsion (DEP) can be leveraged for augmented lift and vehicle control. Six electric ducted fan (EDF) array placements were tested by positioning the fans along the leading and trailing edges on the top and bottom surfaces, as well as centered on the chord line in front of and behind the wing. Each fan placement configuration was tested with an array of one, three, and five EDFs to characterize an aeropropulsive extrapolation effect, and the bare wing was tested separately to provide baseline aerodynamic measurements. The results compare the longitudinal forces and moments for each configuration by analyzing the combined aeropropulsive interaction effects, and offer valuable insight into considerations for fan placement along a wing to enable the benefits of DEP integration.

Nomenclature

C_A = body-axis axial force coefficient

C_D = wind-axis drag coefficient

C_L = wind-axis lift coefficient

C_l = body-axis rolling moment coefficient

C_m = body-axis pitching moment coefficient

C_N = body-axis normal force coefficient

C_n = body-axis yawing moment coefficient

C_X = body-axis x-force coefficient

C_Y = body-axis side force coefficient

Presented as Paper 2025-1453 at the AIAA SciTech 2025 Forum, Orlando, FL, 6–10 January 2025.
*Research Aerospace Engineer, Flight Dynamics Branch, weinstein.rosie@gmail.com, AIAA Member.
†Research Aerospace Engineer, Flight Dynamics Branch, vinspada@hotmail.com, AIAA Member.
‡Research Aerospace Engineer, Flight Dynamics Branch, benjamin.m.simmons@nasa.gov, AIAA Member.

D = fan inlet ring maximum diameter, in

d = fan blade diameter, in or ft

F = fan

F_{pos} = fan position

N = normal force, lbf

n = fan rotational speed, rev/s

n_F = number of fans

PM = pitching moment, ft-lbf

$\bar{q}$ = freestream dynamic pressure, lbf/ft^2

T = thrust, lbf

V_∞ = freestream velocity, ft/s

α = angle of attack, deg

η = motor pulse width modulation command, μs

I. Introduction

There is strong global interest in developing more sustainable approaches to air travel by exploring, advancing, and merging varied technologies to reduce emissions and improve aircraft operating efficiencies. From air taxis to commercial transports, many vehicles rely upon the use of electrified aircraft propulsion (EAP), along with advancements in aerodynamics, materials, energy management, and battery technology, to develop a hybrid-electric or fully electric vehicle [1].

The electrification of aircraft has prompted the transformation of future vehicle designs from traditional single- or dual-engine fuel-burning vehicles to ones in which the thrust is distributed in an array across several smaller propulsive units that are integrated into the wing. A distributed electric propulsion (DEP) approach offers numerous potential advantages, such as a higher total capture area and subsequent propulsive efficiency improvements; allowance for flexible and strategic fan placement; aeropropulsive interactions to be favorably leveraged, such as through boundary-layer ingestion (BLI); and propulsion-based control allocation, which could reduce the need for control surfaces and decrease the size of the vertical tail. These benefits must also be balanced with the tradeoffs of structural integration challenges, added complexity of system integration, battery weight and storage, increased drag, and electric power requirements [2].

There is a wide trade space for the design and integration of DEP into both conceptual and developed flight vehicles, with variations seen across the propulsion unit and the associated thrust, acoustic, and efficiency characteristics; blade diameter-to-chord-length ratio; number of propulsors; spacing between propulsors; position of the array relative to the wing; and integration into the wing surface. In particular, this work investigates the placement of electric propulsor arrays along the chordwise and vertical directions of a wing and considers propulsor placement specifically at the leading edge (LE) and trailing edge (TE) across the upper and lower wing surfaces. These fan placement factors vary considerably across different flight vehicles [2], with several aircraft listed below and a subset shown in Fig. 1:

1) LE Top: ONERA AMPERE (concept filed via Soleau envelope) [3] and Whisper Aero Jet*
2) LE Centered: NASA X-57 [4], Electra Demonstrator,† and Flexcraft VERA II‡
3) LE Bottom: ESAero ECO-150 (split-wing configuration) [5]
4) TE Top: Lilium Jet,§ NASA N3-X [6], and NASA Cruise Efficient Short Take-Off and Landing (CESTOL) [7]
5) TE Centered: Kitty Hawk Heaviside¶
6) TE Bottom: ONERA DRAGON [8]

*Information available online at https://www.whisper.aero/aviation [retrieved: 3 November 2024].
†Information available online at https://www.electra.aero/ [retrieved: 3 November 2024].
‡Information available online at https://evtol.news/flexcraft-vera-ii [retrieved: 3 November 2024].
§Information available online at https://evtol.news/lilium-jet-16-seater/ [retrieved: 3 November 2024].
¶Information available online at https://evtol.news/kitty-hawk-heaviside/ [retrieved: 3 November 2024].

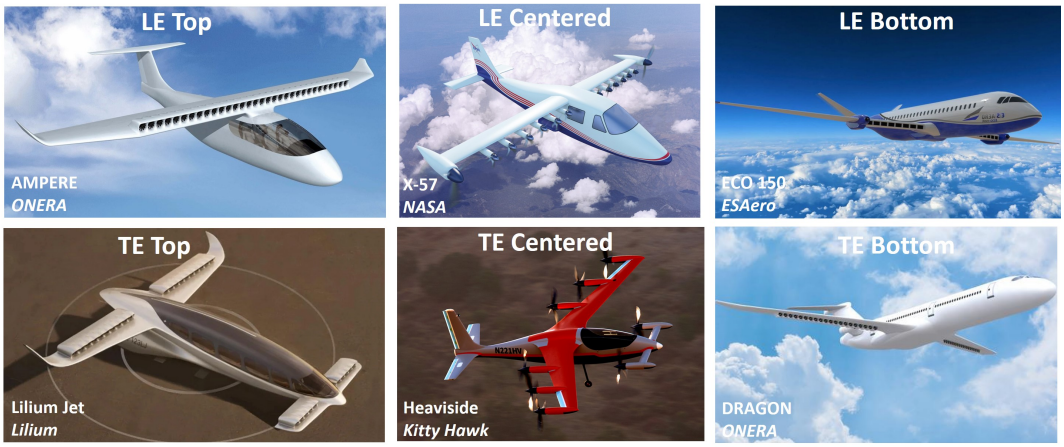


Fig. 1 DEP placed in various positions along the wings for different flight vehicles (all images reproduced with permission from the associated sources).

Note that the centered configurations tend to use open propellers as opposed to the ducted fan approaches shown for the other vehicles. These configurations also often use pylons and a slightly offset vertical positioning of the fans from the center of the wing.

As DEP is considered for new concepts and vehicles, a system-level assessment and integrated design are necessary to develop a vehicle with the desired performance characteristics. Design constraints include the purpose of the flight vehicle, flight conditions and speeds, acoustics, manufacturability, structural integration, available power, and cost. Despite the vehicle-specific nature of the final design, a general understanding of how the DEP placement may affect the vehicle aerodynamics and the resulting aeropropulsive interactions could provide early insight and narrowing of the design space.

Previous related work used wind tunnel testing to study the aeropropulsive interactions due to electric ducted fan (EDF) arrays. In Ref. [9], the aeropropulsive and propulsor cross-coupling effects across throttle setting and angle of attack were analyzed for an array of five EDFs placed at the TE above the wing, with a particular focus on measuring and understanding the BLI effect. Another wind tunnel test on a semispan Cirrus SR22T geometry with four EDFs embedded on the TE upper surface considered the steady and unsteady forces and moments due to changes in angle of attack and fan speed [10]. For vertical takeoff and landing (VTOL) and short takeoff and landing (STOL) applications, the integration of a single EDF at the LE and TE on top of a wing was investigated to study the aeropropulsive effects on thrust, normal force, and power measurements from the fan [11]. In Ref. [12], the changes in EDF performance were considered for the LE and TE positions on both the top and bottom of the wing to measure the effect on thrust coefficient, pitching moment, and power loading.

Outside of wind tunnel testing, a computational study using OVERFLOW investigated a TE top positioning of a five-fan EDF array on each wing of a subscale testbed, with a custom inlet designed to improve the BLI effect [13].

A framework developed in Ref. [14] uses computational modeling and optimization algorithms to study and narrow down a wide range of DEP designs. Finally, a flight test campaign described in Ref. [15] developed a subscale research platform for aeropropulsive system identification and DEP flight control research with an array of four EDFs placed at the TE top position on each wing.

Because of the widespread interest in DEP technology and the substantial variation in its utilization, the objective of this work is to provide a better understanding of the considerations for DEP placement on a wing based upon the resulting aeropropulsive effects at low-speed subsonic conditions. The highly integrated nature of DEP results in complex aeropropulsive interactions that cannot be modeled by a superposition of propulsion and airframe aerodynamic effects. To provide insight for a variety of different DEP arrangements, a wind tunnel test was conducted that varied the position of propulsors along a wing and measured the combined integrated aeropropulsive effects. The Adaptable Distributed Electric Propulsion Testbed (ADEPT) Wing was developed throughout this work and provides a versatile capability for rapidly testing electric propulsors along a wing to experimentally study aeropropulsive and propulsor-propulsor interactions for DEP applications. In this paper, the results from 20 configurations are presented, with EDFs placed along the LE and TE on the top and bottom surfaces and centered on the chord line in front of and behind the wing. Each fan placement configuration was tested with an array of one, three, and five EDFs.

The remainder of this paper is organized as follows: Section II describes the model design and manufacturing approach, power distribution, wind tunnel setup, and instrumentation. Section III discusses the wind tunnel experiment design and data evaluation approach, including a description of the configurations and test factors. The wind tunnel test results for the bare wing, the static propulsive effects, and the aeropropulsive effects are presented in Secs. IV, V, and VI, respectively. Finally, Sec. VII discusses the conclusions of this work.

II. Experimental Setup

This section describes the DEP hardware that was selected for this study; the model design, manufacturing, and checkouts; the power distribution required to run the test; and the wind tunnel setup, instrumentation, and measurements recorded.

A. DEP Hardware

The Jetfan 130 Pro EDF Unit with a TFL SSS 56114 500 Kv brushless DC (BLDC) motor and Advanced Power Drives (APD) UHV 20S electronic speed control (ESC) was studied as a commercial-off-the-shelf (COTS) fan assembly through analysis and characterization performed in Ref. [16]. The same hardware was also used for the aeropropulsive interaction test conducted in this work. Each motor is rated for 7 kW of maximum continuous DC power and was operated at 75 V. A COTS inlet ring was used for each fan to improve the inlet flow characteristics and fan efficiency. An aluminum heat sink alleviated thermal loads from the motor, and the EDF was dynamically balanced by the supplier

before testing. The EDF is shown in Fig. 2, with the attributes summarized in Table 1.

Past work [16] characterized the EDF assembly and evaluated its performance. The test included one-factor-at-a-time (OFAT) and design of experiments (DOE) approaches implemented across a range of fan speed, voltage, freestream dynamic pressure, and incidence angle. The results included a static motor model, a dynamic motor model, an EDF thrust model, and a power consumption model. Negligible torque was measured due to the flow straightening provided by the fan outlet guide vanes. Both the modeling results, as well as the hardware and software infrastructure developed through the single-fan-characterization, supported the test and analysis discussed in this paper.



Fig. 2 Jetfan 130 Pro EDF unit.

Table 1 Jetfan 130 Pro EDF attributes

Property	Value
No. of blades	10
No. of stators	7
Blade diameter, d	5.11 in
Inlet ring maximum diameter, D	6.5 in

B. Wing Design and Manufacture

A rectangular wing planform was designed with a constant airfoil for the ADEPT Wing in this work. The tradeoffs among design parameters of span, chord, aspect ratio, and surface area were all considered within the constraints of the test section size. Driving factors that influenced the choice of design parameters included applicability to an electrofan commercial transport demonstrator aircraft [17–19], maximum span for DEP mounting, manufacturability, structural integrity, and balance load limits. Although a larger span was desirable to mount more fans at wider spacings, a 6 ft span was chosen to avoid wall effects in the 12-ft-wide test section, ensure minimal variation in tunnel airspeed across the span based upon a flowfield survey across the cross section of the tunnel, mitigate vibrations, and reduce blockage at high angles of attack. A 2 ft chord was selected to reduce tunnel blockage and maximize the aspect ratio to more closely resemble a transport vehicle. A constant subsonic NACA 23015 airfoil was chosen for the wing to limit the manufacturing complexity and allow sufficient thickness for fan and wiring containment. Test section blockage was investigated at the beginning of the test, with no significant effects seen. The ADEPT Wing properties are summarized in Table 2.

Table 2 ADEPT Wing properties

Factor	Value
Span, b	6 ft
Chord, $\bar{c}$	2 ft
Reference area, S	12 ft^2
Aspect ratio	3
Airfoil	NACA 23015

The ADEPT Wing was designed in a modular manner to customize the fan positioning, number of fans, and spacing between the fans, as well as to facilitate rapid reconfiguration during testing. To also accommodate a future propulsor-propulsor interaction study, several different wing sections were 3-D printed and configured to slide onto the internal rig structure, with the varying widths designated as a function of the maximum diameter of the inlet ring, $D = 6.5$ in. Wing sections of $1D$ with an internal gap allowed each fan to be mounted to the rig within the section at the LE or the TE on the upper or lower surface; spacer sections of $D/2$, $D/4$, and $D/8$ provided an adjustable spacing between the fans with the resolution of $D/8$; and wingtip sections provided at least $2D$ of spacing between the outboard fans and the wingtip to avoid tip interaction effects. The center fan wing section had a wider gap than the other fan pieces to accommodate the balance integration. Several 3-D printed plugs contoured to the airfoil shape were used to fill the openings in the fan sections for locations outside of the fan placement, fasteners secured the wing sections to the framing of the wing structure, and aluminum tape covered any holes and gaps between sections. A narrow channel was designed in the 3-D printed wing sections behind the rear spar to allow the motor wiring to enter the model at the center rib and be passed along the span to each fan position. Although multiple fan spacing configurations are possible with the ADEPT Wing, only the $0D$ configurations are discussed in this work. A CAD model of the wing assembly for a $5F$ configuration with $0D$ spacing is shown as an example in Fig. 3a.

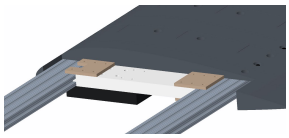
The structural frame is displayed in Fig. 3b and was constructed using two 1×3 in extruded aluminum T-slot framing spars that were integrated into the wing sections along the chord line. Waterjet aluminum components included a central rib, a model-to-balance adapter, and bolt plates. Nonstructural 1×1 in T-slot framing ribs were placed between the spars through the EDF fan sections, upon which the plugs rested. T-slot framing fasteners were deemed insufficient for the propulsive and wind tunnel vibration loads, so through holes were drilled into the spars at every EDF position considered in the design space, and the EDFs were attached with a mounting band and custom aluminum brackets and plates, as shown in Fig. 3c. For the Top and Bottom fan placements, the EDFs were mounted directly to the spars, with the thrust vector therefore pointed along the chord line of the wing. For the LE and TE Centered positions, the EDFs

were mounted to pylons connected to the bottom of the wing spar with custom waterjet brackets, as shown in Fig. 3d, with the thrust vector also parallel to the chord line for these configurations.

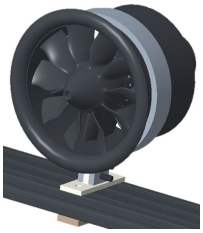
To accommodate fan placement on both the top and bottom of the wing and to limit sting interference with the fans, a bent sting was configured to enter the wing near the quarter chord with a balance-to-model adapter that could be placed on both sides of the center rib. For the configurations with the fans placed on the top of the wing, as well as centered along the chord line, the sting entered the model from the bottom. For the fan positions on the bottom of the wing, the sting was rotated 180 deg and entered the model from the top.



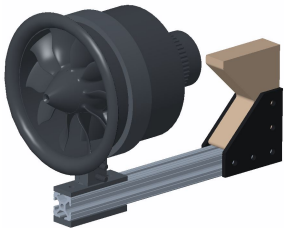
(a) 3-D printed wing sections including fan placement parts (dark gray) and associated plugs (white), spacers (light gray), and wingtips (black).



(b) Internal rig structure consisting of two spars, a center rib, a balance adapter, and attachment plates.



(c) EDF mounted to the wing spar with a mounting band, bracket, and plate.



(d) EDF mounted at the LE Centered position on a pylon.

Fig. 3 ADEPT wing design and integration for rapidly reconfigurable DEP testing.

C. Power Distribution

Three 10 kW Magna SL 80-125/480+LXI power supplies were selected to provide a total of 30 kW of DC power to the motors. These compact, lightweight power supplies collectively provide a modular setup that could be arranged in series or in parallel for varied applications. For this test, the power supplies were run in parallel by pooling the DC output into a distribution box, where the ESCs were connected. As discussed in Sec. II.A, the motors were run at 75 V, with up to 375 A available to be distributed across the five fans.

The positioning of the distribution box and the ESCs between the power supplies and the motors, and the associated wire lengths and gauges, were carefully studied across safety, efficiency, and signal quality considerations, with the final layout shown in Fig. 4. The power supplies, distribution box, and ESCs were mounted together on a cart in an anteroom beneath the test section, with minimal DC wire length connecting them. This arrangement safely secured the distribution box and ESCs outside of the test section, allowed for active ESC cooling, and reduced voltage ripple and voltage drop. A 120 V, 3600 μF capacitor bank was also used for each ESC during the testing to mitigate voltage ripple and improve

the DC signal quality, and the ESCs were cooled with airflow from individual 12 V fans mounted to each of them.

The AC wiring connecting the ESCs to the motors was consequently lengthened to transfer power from the anteroom to the floor of the test section and then along the sting to the model. The longer wire lengths necessary in this test, compared to the single-fan-characterization in Ref. [16], created a less efficient setup and a consequent voltage drop seen by the motors. The motor wiring was routed along the sting to enter the model and was placed as far as possible from the balance to mitigate electromagnetic interference (EMI) effects.

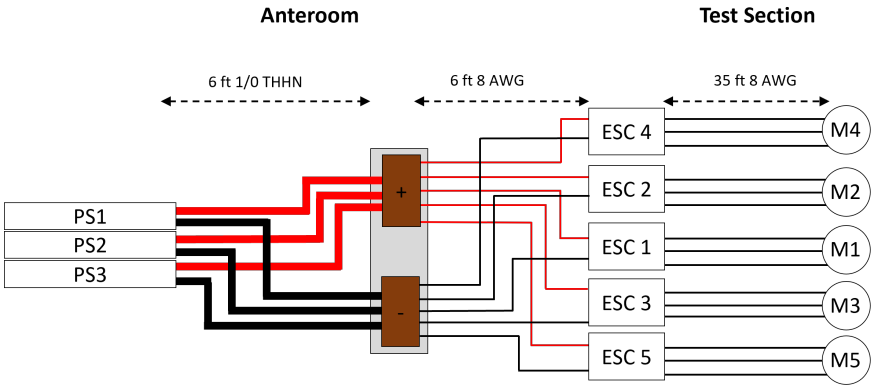


Fig. 4 Power distribution from the power supplies to the motors.

D. Wind Tunnel Setup and Instrumentation

The test was conducted in the NASA Langley 12-Foot Low-Speed Tunnel, which is an atmospheric-pressure tunnel with a 12 ft octagonal test section. The dynamic pressure can be manually set from the control room, and the sting position and fan speed can be automatically controlled through the data acquisition system (DAS), corresponding to each test point assignment. Time-averaged as well as time-history data were recorded for each measurement over a 5 s interval.

A six-component strain-gage balance was placed on a bent sting and connected to an adapter that mounted onto the wing center rib on the top or bottom. The analog channels included balance forces and moments (with the model coordinate system shown in Fig. 5); tunnel air parameters such as dynamic pressure, atmospheric pressure, and tunnel temperature; and angle of attack. These signals were recorded at 2500 Hz for each test point to allow for detection of the EDF rotational frequencies in the balance measurements. The power supplies were programmed in a master/slave configuration to set the applied voltage and current limits from the DAS, as well as to transmit voltage and current data to the DAS to be recorded during the test.

The ESC accepts a standard pulse-width modulation (PWM) input command η, which is a rectangular wave with a pulse width that is modulated to describe the throttle setting, where $\eta = 1100$ μs corresponds to a throttle at 0%, and $\eta = 1900$ μs designates a throttle setting of 100%. The ESC also transmitted several data streams at 50 Hz, including motor rotational speed, ESC temperature, voltage, current, motor duty, and throttle duty, through the universal

asynchronous receiver-transmitter (UART) output pins. A microcontroller setup was programmed and used as the interface to send the commanded PWM signals to the ESC from the DAS, as well as to transmit the UART data back to the DAS to be recorded during testing. To accommodate bidirectional communication between the DAS and five ESCs, the microcontroller setup consisted of an Arduino Giga, which served as the main board for connectivity to the DAS; an Arduino Mega to offer additional serial communication inputs; and a custom distribution board to provide optical isolation between the ESC PWM and UART pins and to distribute the 5 V power and ground pins across the five ESCs. Strip charts were programmed to display the PWM commands, ESC data, and power supply data in real time to monitor the fan performance, ESC temperatures, and data quality in the wind tunnel control room.

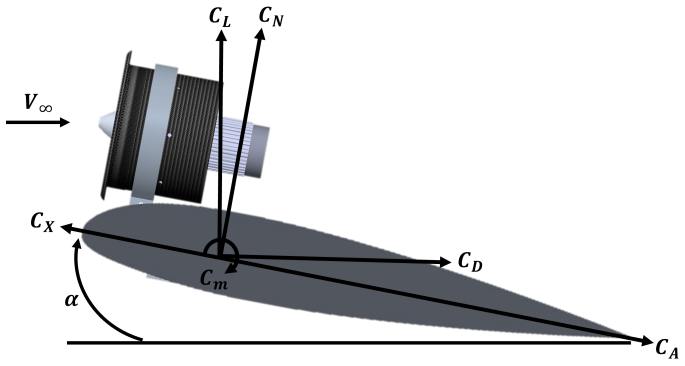


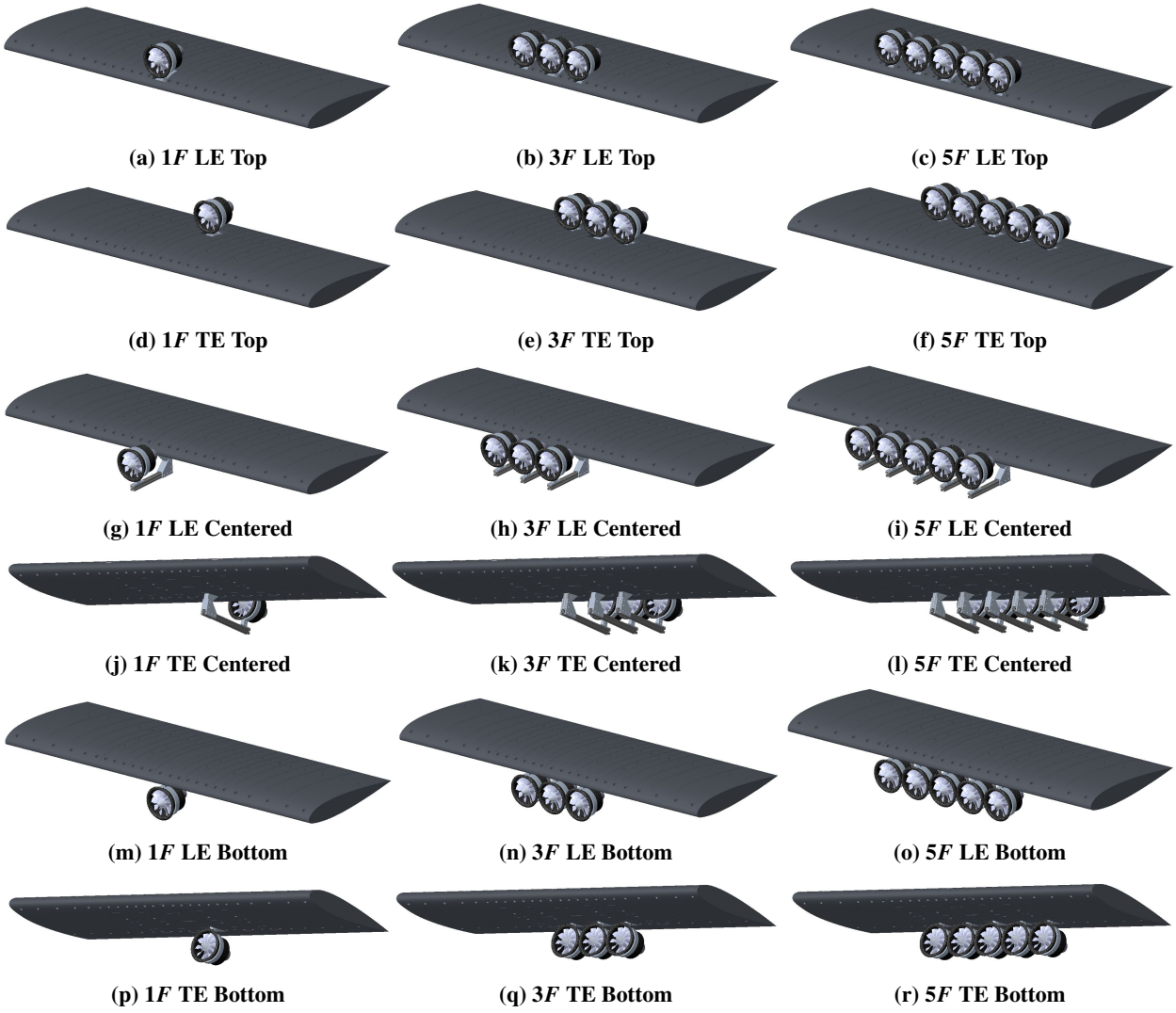
Fig. 5 Model coordinate system in wind and body axes with the moment reference center placed at the quarter chord.

III. Experiment Design and Data Evaluation

The results from 20 configurations tested with the ADEPT Wing are discussed in this paper, consisting of the bare wing with the sting mounted on the top and bottom, and EDFs placed at the LE Top, TE Top, LE Centered, TE Centered, LE Bottom, and TE Bottom positions. Each fan placement configuration, designated as F_{pos}, was tested with an array of one, three, and five EDFs at $0D$ spacing, as shown in Fig. 6. The same fan, motor, and ESC were used for each position across the array for all of the F_{pos}.

The test factors are summarized in Table 3 and included the freestream dynamic pressure, angle of attack, and up to five independent EDF throttle commands that were run uniformly for the results presented in this paper. The upper throttle setting was limited by power availability to $\text{PWM}_{\text{max}} = 1825\ \mu$s, or 24,400 rpm, for the $1F$ and $3F$ cases, and $\text{PWM}_{\text{max}} = 1750\ \mu$s, or 22,600 rpm, for the $5F$ cases.

For each configuration, a series of sweeps was completed to explore the design space and investigate the trends in each measurement across a single factor. A wind-off throttle sweep was performed for each fan within each configuration, as well as with all fans collectively within the configuration, as a measurement checkout and to observe any static interaction effects. A wind-on throttle sweep was performed at 0, 2, and 10 deg angle of attack, corresponding to



(a) 1*F* LE Top **(b) 3*F* LE Top** **(c) 5*F* LE Top**

(d) 1*F* TE Top **(e) 3*F* TE Top** **(f) 5*F* TE Top**

(g) 1*F* LE Centered **(h) 3*F* LE Centered** **(i) 5*F* LE Centered**

(j) 1*F* TE Centered **(k) 3*F* TE Centered** **(l) 5*F* TE Centered**

(m) 1*F* LE Bottom **(n) 3*F* LE Bottom** **(o) 5*F* LE Bottom**

(p) 1*F* TE Bottom **(q) 3*F* TE Bottom** **(r) 5*F* TE Bottom**

Fig. 6 CAD rendering of DEP configurations tested with the ADEPT Wing at 0*D* spacing.

Table 3 Input test factors and sweeps for each configuration

Type	$\bar{q}$ (lbf/ft^2)	α (deg)	PWM (μs)
Static	0	0	[1100, PWM$_{\max}$]
Constant α	3	0	[1100, PWM$_{\max}$]
Constant α (cruise)	3	2	[1100, PWM$_{\max}$]
Constant α (takeoff)	3	10	[1100, PWM$_{\max}$]
Constant PWM (25% throttle)	3	[-4, $\alpha_{\max}$]	1500 ($\hat{J}$ = 2.16)
Constant PWM (50% throttle)	3	[-4, $\alpha_{\max}$]	1600 ($\hat{J}$ = 2.62)
Constant PWM (75% throttle)	3	[-4, $\alpha_{\max}$]	1700 ($\hat{J}$ = 3.03)

aligning the thrust vector with the freestream velocity and an approximation of the nominal cruise angle of attack and takeoff conditions for typical commercial transport aircraft, respectively. For the throttle sweeps performed at a constant

angle of attack, each of the fans was run at the same open-loop PWM command settings, and these sweeps are described or plotted across the nondimensional fan speed,

$$\hat{J} = \frac{nd}{V_\infty} \tag{1}$$

to normalize the fan speed results and provide an improved comparison. The nondimensional fan speed $\hat{J}$ is the inverse of advance ratio $J = V_\infty/nd$, and was shown in Ref. [20] to characterize propulsive effects and propulsion-airframe interaction effects when presenting results using the standard aircraft force and moment coefficients because of its consistency with the normalization of propeller aerodynamics. Reference [9] used a similar variable for visualization of the variation of nondimensional force and moment coefficients with fan speed. For results that are plotted across $\hat{J}$ or in which $\hat{J}$ is designated as constant, the average is used across all of the fans in the array and/or collection of runs in a given plot. This was due to minor variations in fan speed among the EDFs.

Finally, angle-of-attack sweeps were performed at constant throttle settings of around 25, 50, and 75% of the maximum throttle within the relevant throttle range. The open-loop PWM commands, as well as the average $\hat{J}$ measured across all of the corresponding angle-of-attack sweeps, are shown in Table 3. The variation in average $\hat{J}$ within each set of sweeps was less than 2.3%. A wide range of angle of attack up to 45 deg was initially specified to observe how the aeropropulsive effects changed the post-stall aerodynamics while limiting the tunnel blockage; however, many of the runs were ended prematurely due to various considerations, including unsteady blade disk loading for fans ingesting separated flow, a lower prioritization of the post-stall aerodynamics after wing departure, and time savings. In particular, several of the TE Top and TE Centered angle-of-attack sweeps were ended prematurely due to the ingestion of separated flow into the fans and the resulting unsteady disk loading that was made apparent by acoustic effects of fan rumbling. This effect was reduced with additional fans and was not noticeable with the TE Bottom fan placements.

All of the wind-on sweeps were performed at a tunnel dynamic pressure setting of 3 lbf/ft^2 (a freestream velocity of 50.2 ft/s at standard sea level conditions and a Reynolds number of 600,000). The sweeps provided a 2-D set of data across the angle-of-attack and throttle variables, with additional categorical dimensions of n_F and F_{pos} included in the data analysis. Given the large number of sweeps that were performed and the total number of factors, there are many ways to visualize the data. Select figures are presented in these results to showcase key effects of the factor variations and to highlight particular insights.

The wind-on results are presented across C_N, C_X, and C_m to investigate the aeropropulsive effects on the longitudinal forces and moments, with the body axes chosen instead of the wind axes to align the results parallel and perpendicular to the fan thrust axis, which was parallel to the chord line of the wing. This allows the aeropropulsive interactions in the normal force direction to be independent of the thrust vector contribution. The variables C_N and C_X were also selected for easier interpretation and to study how an increase in fan speed may cause corresponding favorable increases in these

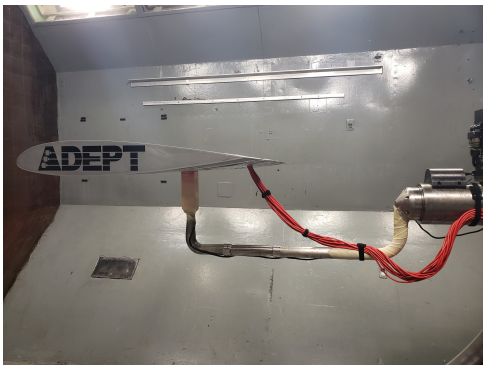
forces. The moment reference center for the C_m results is placed at the wing quarter chord. Figure 5 displays the forces and moments discussed throughout this work relative to the model, and Table 4 lists the uncertainty values for the aerodynamic coefficients at $\bar{q}$ = 3 lbf/ft^2 based upon a 95% confidence interval for the balance instrument uncertainty. The data trends and inferences provided in the ensuing discussions take into account these uncertainty estimates, and results are considered marginal or inconclusive when sufficient distinctions in the data are not apparent.

Table 4 Uncertainty for aerodynamic coefficients at $\bar{q}$ = 3 lbf/ft^2 based upon a 95% confidence interval for balance measurements.

Coefficient	Value
C_N	0.007
C_X	0.003
C_m	0.001

IV. Bare Wing Aerodynamics

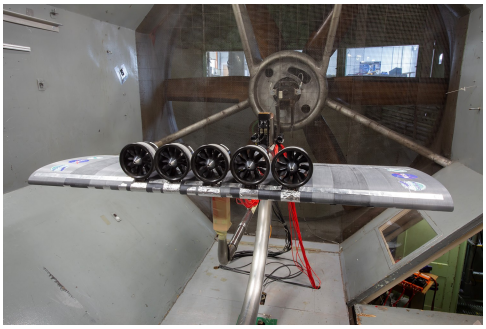
The Bare Wing aerodynamics were characterized separately for the Top and Centered fan positions, as shown in Fig. 7a and designated Bare Wing Top, and for the Bottom fan positions, as shown in Fig. 7b and designated Bare Wing Bottom, due to the different baseline aerodynamics expected for each sting integration position. Figure 7 also shows the fan integration into the wing at the respective sting position for the $5F$ configurations.



(a) Bare Wing Top



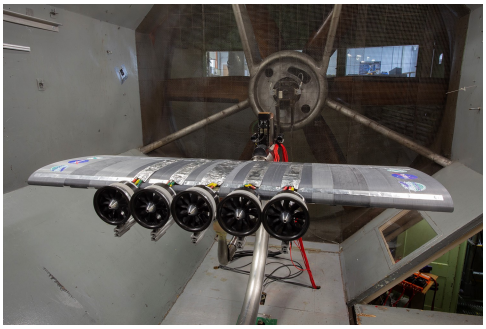
(b) Bare Wing Bottom



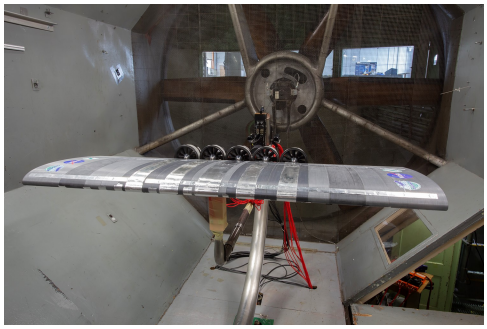
(c) 5*F* LE Top



(d) 5*F* TE Top



(e) 5*F* LE Centered



(f) 5*F* TE Centered



(g) 5*F* LE Bottom



(h) 5*F* TE Bottom

Fig. 7 Bare Wing and 5*F* configurations tested with the ADEPT wing in the 12-Foot Low-Speed Tunnel.

The forces and moments measuring the Bare Wing aerodynamics for each setup across two repeated runs are shown in Fig. 8. The isolated wing is identical in both configurations, so the measured differences in the aerodynamics are attributed to the effect of the sting entering the pressure or the suction side of the wing. The Bare Wing Top C_N and C_X results match closely with predictions from Digital DATCOM [21]. In contrast, the placement of the sting on the upper surface of the wing has a substantial effect, seen as a decrease in C_N below stall, a reduction in C_{N_α}, a horizontal shift of +5 deg in C_X, and a bias in C_m across much of the angle-of-attack range. The slope change beginning around an angle of attack of 2 deg in C_m is also apparent in C_N as the data deviate further from the Bare Wing Top results at that point. The DATCOM results did not predict C_m well for either Bare Wing configuration. The repeatability across the linear angle-of-attack range for both configurations was excellent.

Because the aerodynamic predictions matched the Bare Wing Top C_N and C_X results well across low angles of attack, it is assumed that the Bare Wing Top sting integration had minimal interference effects, whereas the interference of the sting on the suction side of the wing for the Bare Wing Bottom case was notable. Experimental approaches using a dummy sting or high-fidelity computational fluid dynamics simulations could have helped to better understand and quantify the sting effect on the flowfield and the wing aerodynamics. However, this further analysis was considered out of scope for the purpose of this study, which focused on comparing the effects of the integrated fan configurations relative to the respective baseline wing.

The lateral-directional forces and moments for the DEP configurations are not presented in these results but were used during the test to determine and compare the wing departure points, and for checkouts to ensure that the fans were mounted in line with the balance to achieve minimal magnitudes.

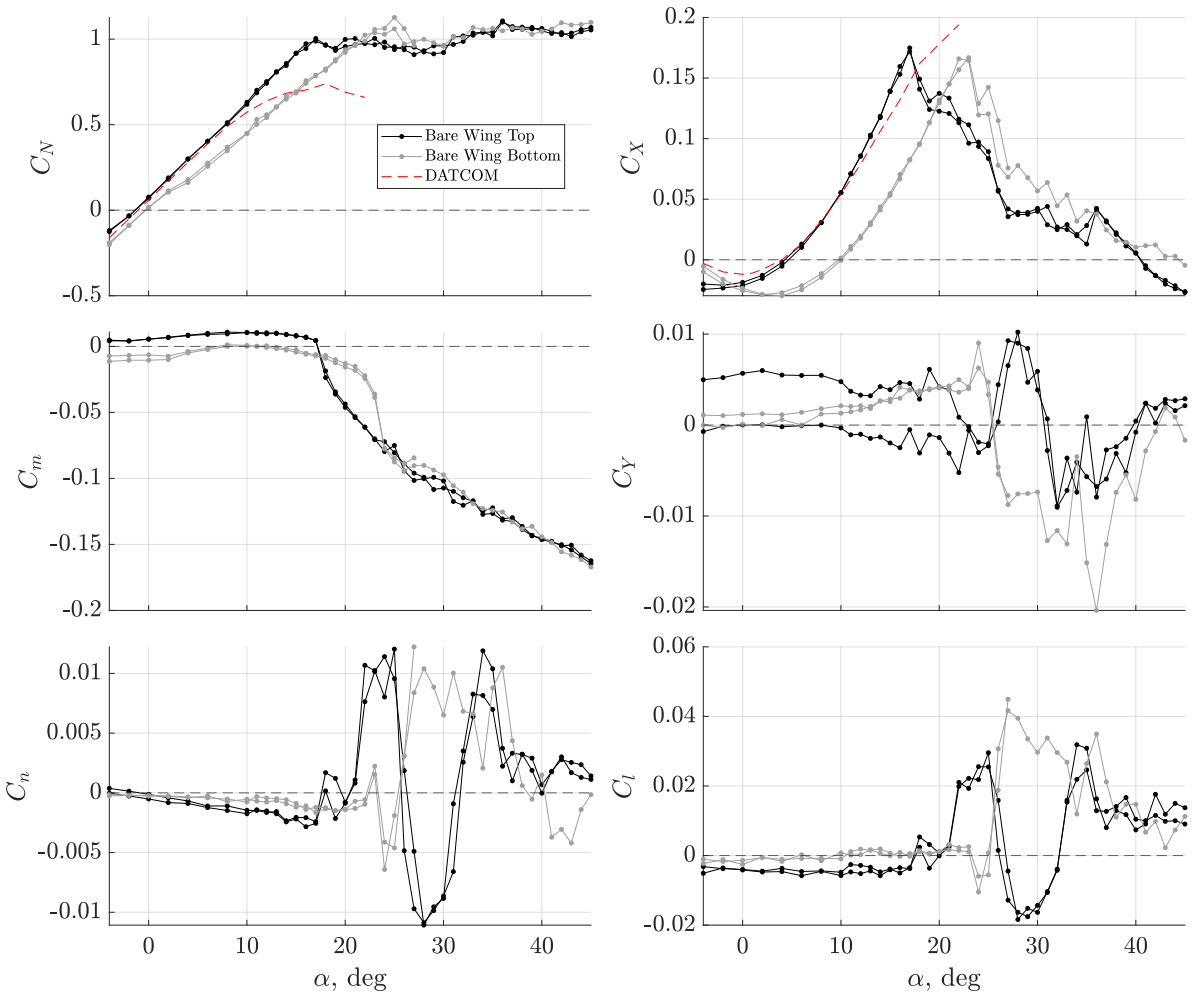


Fig. 8 Baseline body-axis aerodynamics for the Bare Wing Top and Bare Wing Bottom configurations.

V. Static Propulsive Effects

For each configuration, a static throttle sweep was performed using each fan in the array individually as a measurement check on the force, moment, and power readings. This was a valuable checkout that enabled early identification of misalignment in the fan mounting or interference from tape or wiring, as well as provided initial insights into configuration effects and uncertainty estimates.

The static motor response results are displayed in Fig. 9 for all F_{pos} and n_F arrangements, along with the single-fan-characterization results from Ref. [16]. As discussed in Sec. II.C, the extended wire lengths in this test setup resulted in a voltage drop and manifested as a reduction in the fan speed for a given open-loop PWM command compared to the single-fan characterization. Although a full throttle sweep was performed from idle up to the maximum power rating for each motor, the relevant usable throttle range was designated throughout the linear static response with a minimum PWM of 1375 μs, corresponding to 10,500 rpm. Excellent repeatability in the static motor response is seen,

with a maximum difference of 555 rpm. For the EDFs and ESCs used in this work, open-loop PWM commands were sufficient to achieve consistent fan speed results across the range of angle-of-attack positions in both wind-off and wind-on conditions.

The thrust measurements in Fig. 9 show approximately a 20% reduction in thrust for the LE Centered position compared to all of the other configurations due to the effect of the wing blockage directly behind the fans. This reduction in thrust, for the same power consumption, is seen as a large efficiency loss for the LE Centered fan placement. The fans showed a slightly larger thrust output at the TE Centered position compared to the other fan positions and to the single-fan characterization. The static thrust measurements generally match the single-fan characterization results well for all fan positions aside from the LE Centered case. The measurements for side force and rolling moment were small for most sweeps, indicating sufficient fan mounting alignment, with maximum side force within 5% of the maximum measured thrust.

The pitching moment results show a positive value for the Bottom configurations, a negative value for the Top configurations, and close to zero for the Centered configurations. The variation in the Centered position results throughout the paper is attributed to the wing camber, slight misalignments in the pylon attachment mounting, and possibly a pylon interference effect. The thrust prediction from the single-fan characterization was multiplied by the moment arm calculated for the ADEPT Wing between the thrust vector and the center of the rib to which the fans were mounted to produce an estimate of the expected pitching moment values, which match the measured results well. There is a slightly larger magnitude pitching moment for the LE Top and LE Bottom positions compared to the TE Top and TE Bottom positions, respectively.

The normal force production for a single fan was small but trended toward slightly larger magnitudes at higher fan speeds for most cases. There was no clear trend distinguishable across each fan position, other than a positive result seen for the LE Top cases and a negative result for the LE Bottom cases.

A uniform static throttle sweep was also performed across all of the fans in the array to measure the combined propulsor-propulsor effects and to compare this result to a superposition of the forces from each individual fan, as shown in Fig. 10. The net effect is displayed as the summation of forces or moments from each fan run individually subtracted from the combined measurement of all fans run together:

$$\Delta T = T_{\text{total}} - \sum_{i=1}^{n_F} T_i, \qquad \Delta N = N_{\text{total}} - \sum_{i=1}^{n_F} N_i, \qquad \Delta PM = PM_{\text{total}} - \sum_{i=1}^{n_F} PM_i \tag{2}$$

The total thrust results display a grouping of similar measurements for the $3F$ and $5F$ configurations, with the LE Centered position showing a reduction in thrust in comparison, similar to what was shown for the individual fans in Fig. 9. The TE Centered fan position produces the largest amount of total thrust for both sets of n_F configurations. A reduction in total thrust is seen within the operational throttle range for the ΔT results when all fans are running

together compared to the sum of each fan individually, with the largest reductions seen for the TE Bottom cases, the smallest effect seen for the LE and TE Centered positions, and the effect increasing from $3F$ to $5F$. This thrust penalty is understood as a sharing of the inflow across the fan array, with less air available for each fan individually, and is expected to be reduced if the fans are placed at a wider spacing.

Propulsive array effects resulting in static normal force production as air is drawn or blown across the surface of the wing are also shown. The $3F$ and $5F$ LE Top configurations show a significant interaction effect that far exceeds the superposition of the individual fans. Similarly, a notable but smaller effect is also seen in the opposite direction for the LE Bottom case. The TE fan positions resulted in less static normal force production, as the blown-wing effect for the LE fan positions induces a large amount of high-speed airflow across the surface of the wing, whereas the suction effect at the TE is less effective. The LE and TE Centered positions ingest or expel airflow across both the upper and lower surfaces, so a large effect is not expected nor seen there. However, the effect is nonzero because of the wing camber and/or pylon contributions.

Similar to the individual fan results shown in Fig. 9, the pitching moment array effects show a slightly larger magnitude for the LE compared to the TE Top and Bottom positions. The LE Centered fans appear well-aligned with the moment reference center, producing negligible pitching moment, whereas the $5F$ TE Centered position shows a slightly negative pitching moment. The interaction effects for the pitching moment results are small for most cases, but there is a slightly larger magnitude result for the $5F$ TE Top and Bottom positions.

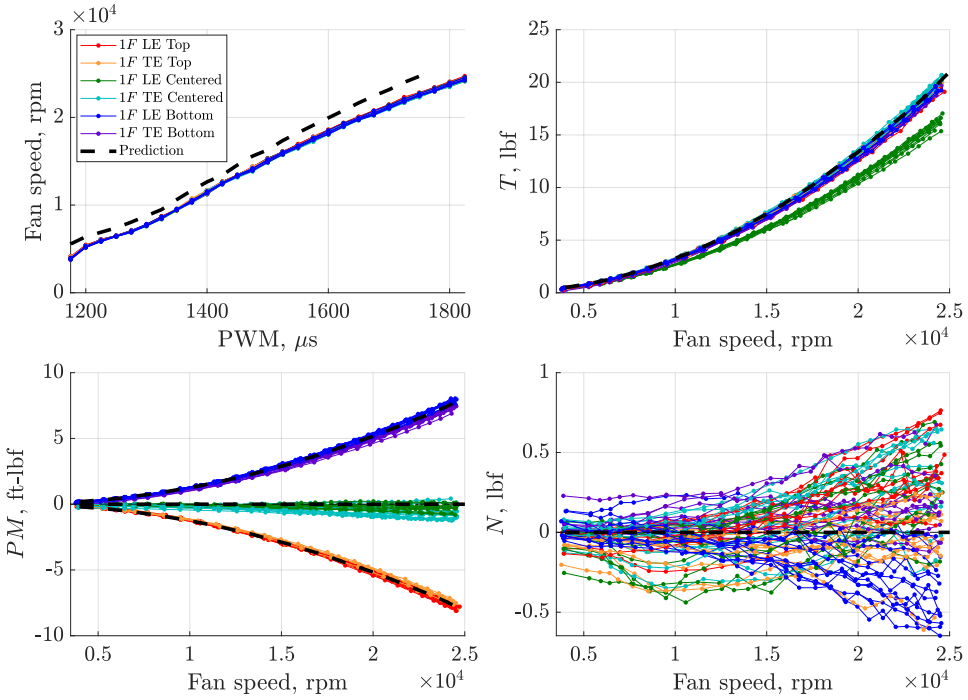


Fig. 9 Static propulsive effects for each fan in the DEP arrays compared to the single fan characterization.

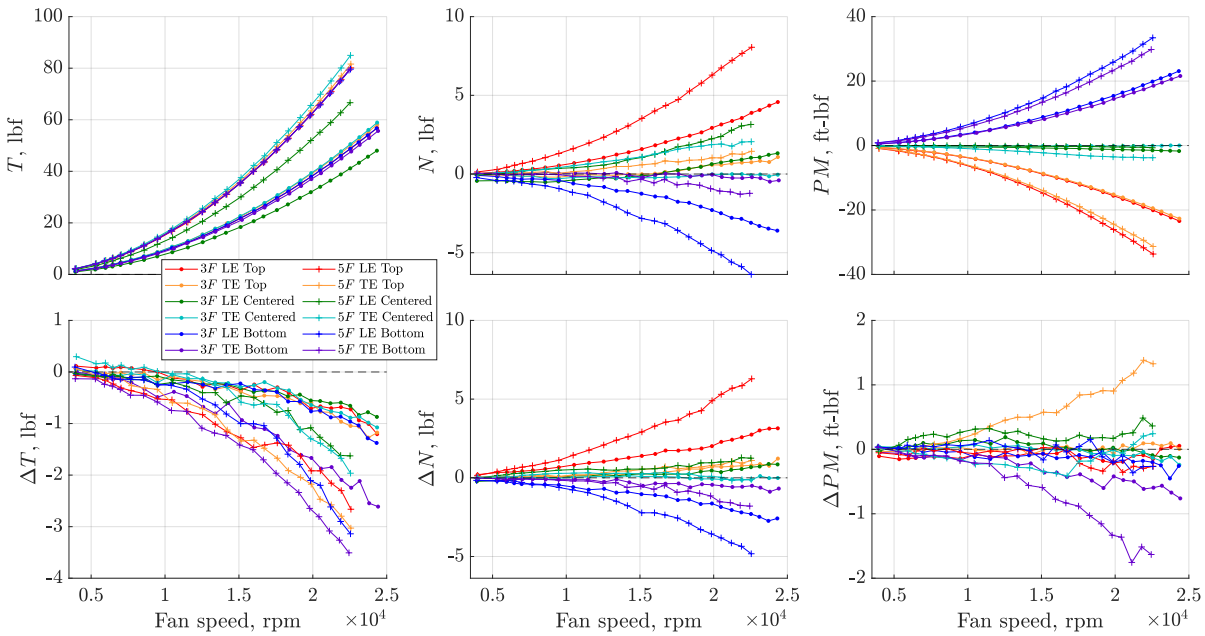


Fig. 10 Static propulsive interaction effects for 3F and 5F arrays.

VI. Aeropropulsive Effects

This section includes detailed analysis studying the aeropropulsive interaction effects for the C_N, C_X, and C_m measurements within and between the fan placement configurations. Several research questions are posed for each force and moment coefficient, and the throttle and angle-of-attack sweeps described in Table 3 are presented to address them.

A. Normal Force Coefficient

The aeropropulsive effects of the fans on the normal force are of particular interest in this work, and the results for the wind-on sweeps were used to discern key insights across the F_{pos}, n_F, angle-of-attack, and throttle factors, using the Bare Wing aerodynamics as a baseline. Many questions can be addressed through comparing the results between F_{pos}, while others are considered separately within each F_{pos}. The following research questions were posed:

1) How does n_F affect C_N across angle of attack (Fig. 11)?
2) Do the aeropropulsive effects on C_N vary linearly with increasing n_F (Fig. 12)?
3) How does $\hat{J}$ affect C_N across the angle-of-attack range, and how effective is fan speed for roll control (Fig. 13)?
4) How do the aeropropulsive effects on C_N vary between F_{pos} (Figs. 14, 15)?
5) How do the aeropropulsive effects on C_{N_α} vary between F_{pos} (Fig. 17)?
6) How does n_F affect C_{N_α} (Fig. 17)?

Question 1 is addressed in Fig. 11, which shows the effect of n_F across angle of attack compared to the Bare Wing for each configuration at $\hat{J} = 3.03$, with similar trends and effects seen for $\hat{J} = 2.62$ and 2.16. The nature of the n_F effect seen on C_N is grouped across the Top, Centered, and Bottom fan placements. The Top configurations produce an increase in C_N with increasing n_F compared to the Bare Wing across all angles of attack. For the Centered configurations, the results are coincident with the Bare Wing at low angles of attack; at mid- to high angles of attack, an increase in slope across n_F leading to an increase in C_N is observed. For the Bottom configurations, a reduction in normal force is seen at low angles of attack, but an increase in slope across n_F presents a crossover point at mid-angle of attack, leading to increased C_N compared to the Bare Wing at high angles of attack. In all cases, there is a stronger blown-wing effect at the LE compared to the suction effect at the TE.

At high angles of attack, n_F increases the maximum C_N compared to the Bare Wing across all fan positions. Although the $1F$ and $3F$ configurations still show a dropoff in C_N at a particular angle of attack close to or beyond that which is seen for the Bare Wing, the $5F$ Top and Centered configurations show a negligible change in slope across the angle-of-attack range tested. The Bottom configurations produce a dropoff in C_N coincident with stall around the same angle of attack as for the Bare Wing, although with a slightly steeper positive slope for the LE position, resulting in higher post-stall magnitudes. It is important to note that although many of the $5F$ results show no reduction in C_N coincident with stall, the lateral-directional forces and moments conveyed wing departure within 5 deg above the Bare Wing stall point. So although these results show normal force being produced even at very high angles of attack, the rest of the wing upon which no fans are mounted is still encountering separated flow, and a vehicle producing augmented lift with DEP may experience the effects of stall in these high angle-of-attack regions.

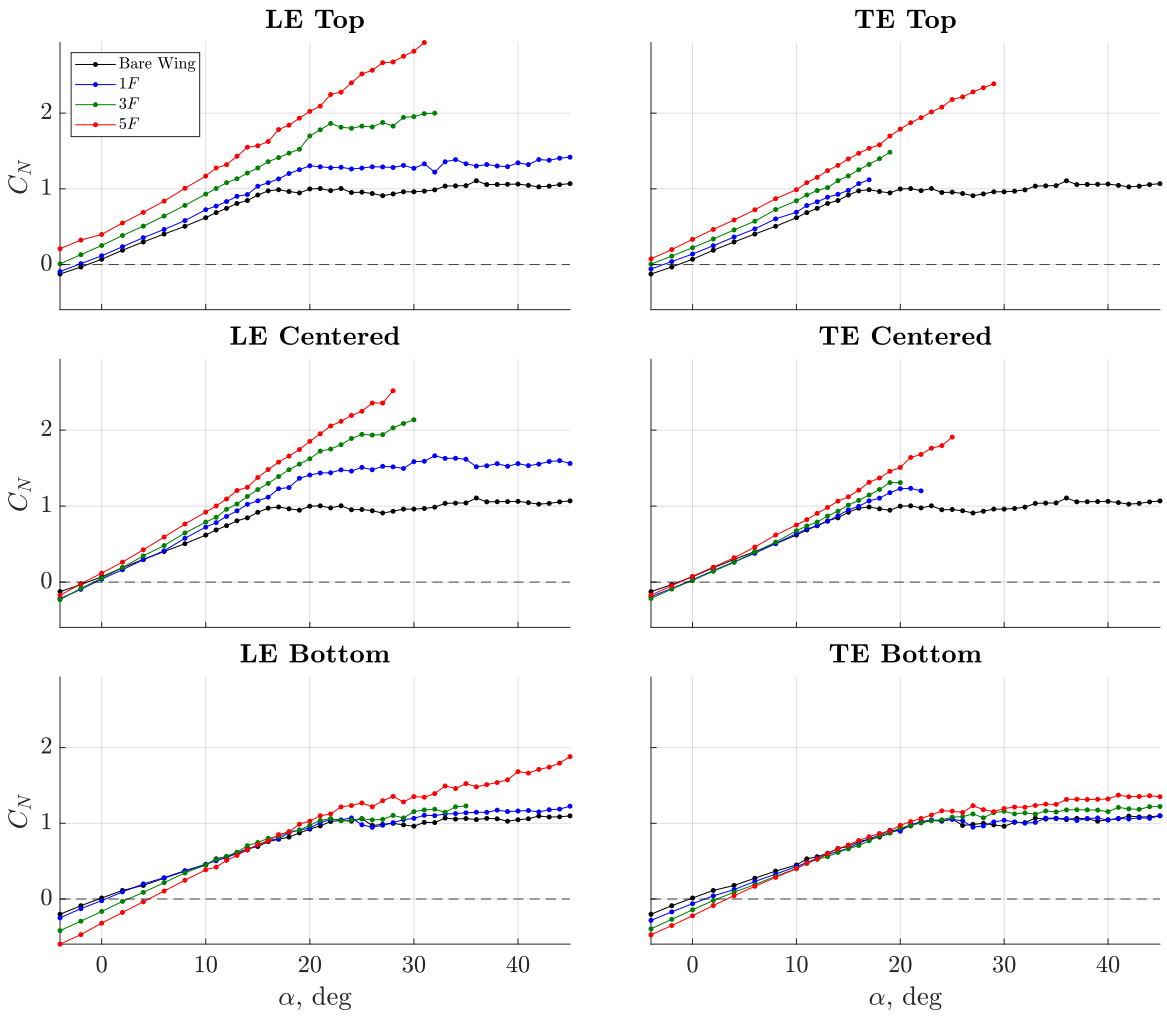


Fig. 11 C_N effect of n_F across angle of attack at $\hat{J}$ = 3.03.

The effect of n_F is further explored through a quantitative assessment to address Question 2 and to determine if the change in C_N compared to the Bare Wing is linear across n_F. Two separate but related aeropropulsive extrapolation effects are considered. First, the results from $1F$ are used to predict the $3F$ and $5F$ results. Because there are assumed to be interaction effects with arrays that have greater than $1F$, a second comparison evaluates the linearity between the $3F$ and $5F$ results alone. If linearity can be assumed (in either case), then the aeropropulsive interaction results may be extrapolated to DEP arrays with greater than five fans; otherwise, caution must be taken to consider applying these results to larger arrays. As the array expands toward the wingtip, the sectional lift decreases significantly and wingtip interaction effects may also become apparent; consequently, these results do not apply to those fan placement configurations.

For an angle-of-attack sweep across a set of discrete points, the DEP effect compared to the Bare Wing aerodynamics is defined as

$$\Delta C_{(\cdot)} = C_{(\cdot)} - C_{(\cdot)_{\text{Bare Wing}}} \tag{3}$$

where $C_{(\cdot)}$ refers to the measured force or moment coefficient for a particular F_{pos} and n_F, and $(\cdot)$ is used to represent the subscripts associated with the force and moment coefficients. The dependence on n_F is then removed by dividing $\Delta C_{(\cdot)}$ by the associated array size n_F to normalize the results and observe if a linear superposition effect is apparent.

The linearity assessment results are shown in Fig. 12 for $\hat{J} = 3.03$, with the same general trends noted for the other fan speeds, as well as for the C_L results. To interpret the plots, if the $3F$ and $5F$ results are coincident with the $1F$ results, then a linear effect is seen from $1F$ to $3F$ and $5F$. If the $3F$ and 5F results are coincident with one another, then a linear effect is apparent from $3F$ to $5F$. If the $3F$ and $5F$ results are above the $1F$ data, an effect on C_N that is greater than a $1F$ linear prediction would account for is seen, or a favorable interaction effect. Correspondingly, data below the $1F$ results indicate that the $1F$ results overpredict what is measured, or there is a penalizing interaction effect. The results are discussed across the low- to mid-angle-of-attack range to focus on the more relevant regions.

For the LE Top, LE Centered, TE Centered, and TE Bottom configurations at low angles of attack, a favorable interaction effect is seen for the $3F$ and $5F$ cases compared to $1F$, i.e., additional normal force is generated beyond what would be linearly extrapolated based on the $1F$ results. Note that these Centered and Bottom configurations produce less normal force than the Bare Wing at low angles of attack. For these cases, a smaller magnitude effect is seen compared to the $1F$ prediction, but because it results in an increased C_N, it is considered a favorable effect. For the LE Bottom case across low- to mid-angle of attack, as well as for the LE Centered configuration above an angle of attack of 8 deg, a penalizing effect is seen where the $3F$ and $5F$ configurations offer a smaller increase in C_N than would be expected from the $1F$ prediction. The TE Top case shows a slight penalizing effect at low angle of attack, and a good $1F$ prediction beyond that. Most of the configurations show an improved $1F$ alignment at higher angles of attack, indicating that a $1F$ linear prediction may be more appropriate closer to climb in those cases, even if it is not at lower angles.

A close linear extrapolation from $3F$ to $5F$ is seen for the Top and Bottom configurations, with a slightly poorer alignment in the Centered configurations. Nevertheless, the $3F$ to $5F$ extrapolation appears much closer and more valid than the $1F$ extrapolation.

To summarize the linearity assessment, in most cases extrapolating from $1F$ to $3F$ or $5F$ arrays is not recommended, as the normalized $3F$ and $5F$ results do not align consistently well with the $1F$ results. The Top configurations offer the best linear prediction, or the smallest array interaction effects. Extrapolation from $3F$ to $5F$ depends on the fan position but generally offers better accuracy than from the $1F$ results.

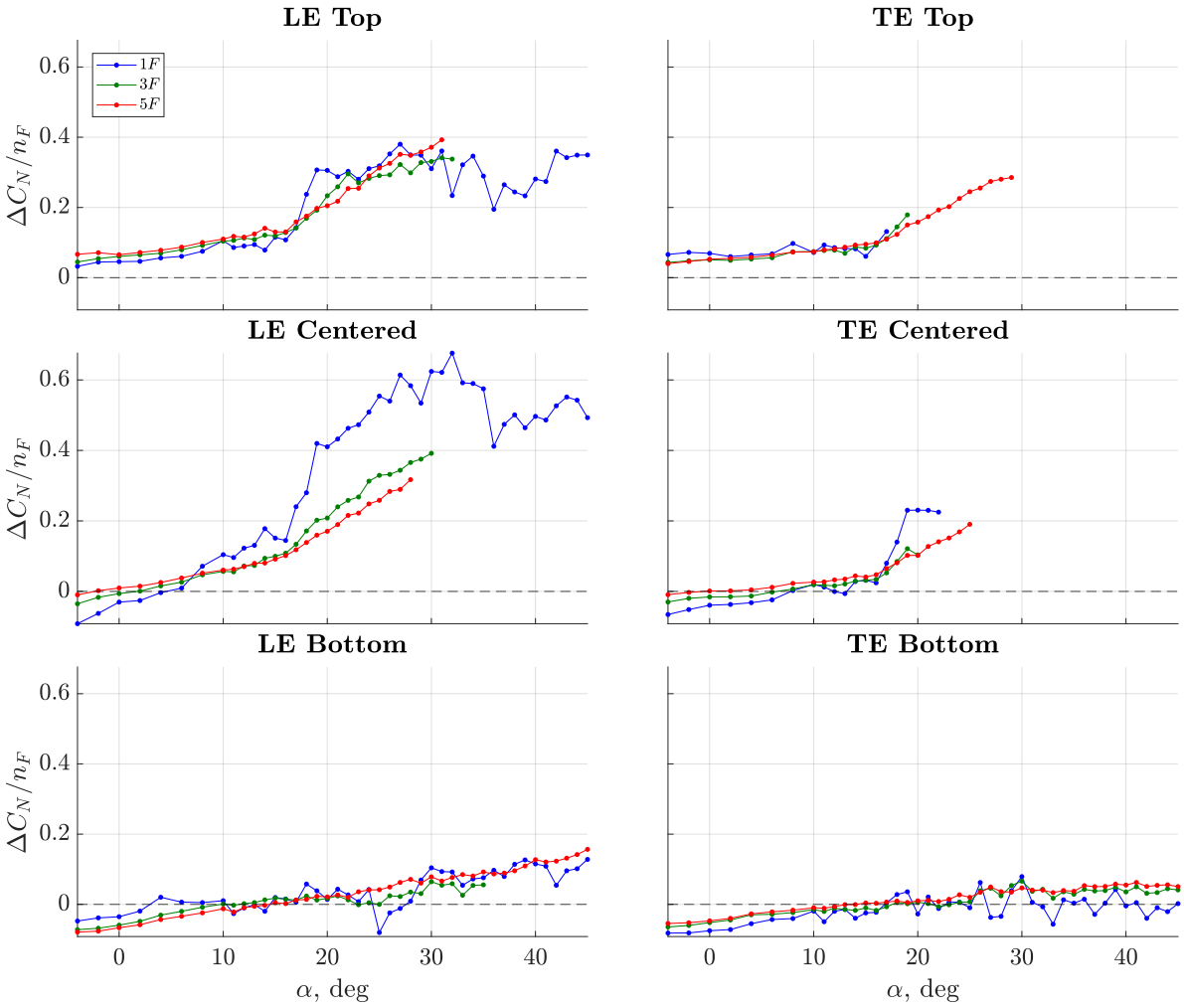


Fig. 12 C_N aeropropulsive extrapolation effect for n_F across angle of attack at $\hat{J}$ = 3.03.

The effect of the fan speed on C_N is considered next for Question 3. The throttle sweep results were studied closely, but key insights were easier to distinguish by merging those results with the angle-of-attack sweeps at constant throttle settings, as shown in Fig. 13 for the $5F$ cases. The trends seen across the Top, Centered, and Bottom configurations for the fan speed effect are very similar to the n_F effect already distinguished in Fig. 11. This is because including additional fans in the array provides increased thrust, similar to what an increase in throttle setting for all of the fans in a given array would offer.

As the fan speed is increased for the Top configurations, an increase in C_N is seen across all of the angle-of-attack setpoints. For the Centered cases, there is a negligible fan speed effect at low angles of attack, and a small fan speed effect beginning at 2 deg for LE Centered and 6 deg for the TE Centered position. Increasing fan speed at low angles of attack for the Bottom configurations results in a reduction in C_N, whereas a negligible effect is seen at mid-angles of attack in these cases. For all configurations across the low- to mid-angle-of-attack range, and particularly evident

for the TE Centered case, the fan speed effect within the 25–75% throttle range designated in Table 3 is small. For configurations and angle-of-attack setpoints where a fan speed effect is more evident, a very large adjustment in throttle setting may be necessary to achieve a notable change in C_N. This effect would be larger if there were more fans in the array.

To summarize the fan speed effect in the context of flight operations, a change in throttle setting to increase airspeed at low angle of attack for the Centered configurations or at mid-angle of attack for the Bottom configurations would result in only a dynamic pressure effect on the dimensional normal force $N = \bar{q}SC_N$, with minimal effect on the C_N contribution. For the other configurations or other angles of attack, a slightly stronger effect on normal force would be realized through the contribution of an adjusted C_N. This also implies that if the fan speed is used for roll control to locally increase the normal force along the wing, there would be regions of angle of attack for the Centered and Bottom configurations at which the effectiveness would be reduced. Adjusting the fan speed for roll control would not be as effective across low angles of attack for the Centered positions and a wide range of mid- to high angles of attack for the Bottom positions. Note that whereas the effect of fan speed on C_N appears overall to be small, there is a much more substantial effect on C_L due to the thrust vector pointing in the vertical direction, so a stronger contribution to augmented lift is still achievable.

Similar trends and effects are seen for the $3F$ configurations at a smaller magnitude, whereas for the $1F$ cases, the fan speed effect is exceedingly small across the low- to mid-angle-of-attack range for all configurations, indicating that a small adjustment in $1F$ fan speed is not sufficient to have a significant effect on C_N.

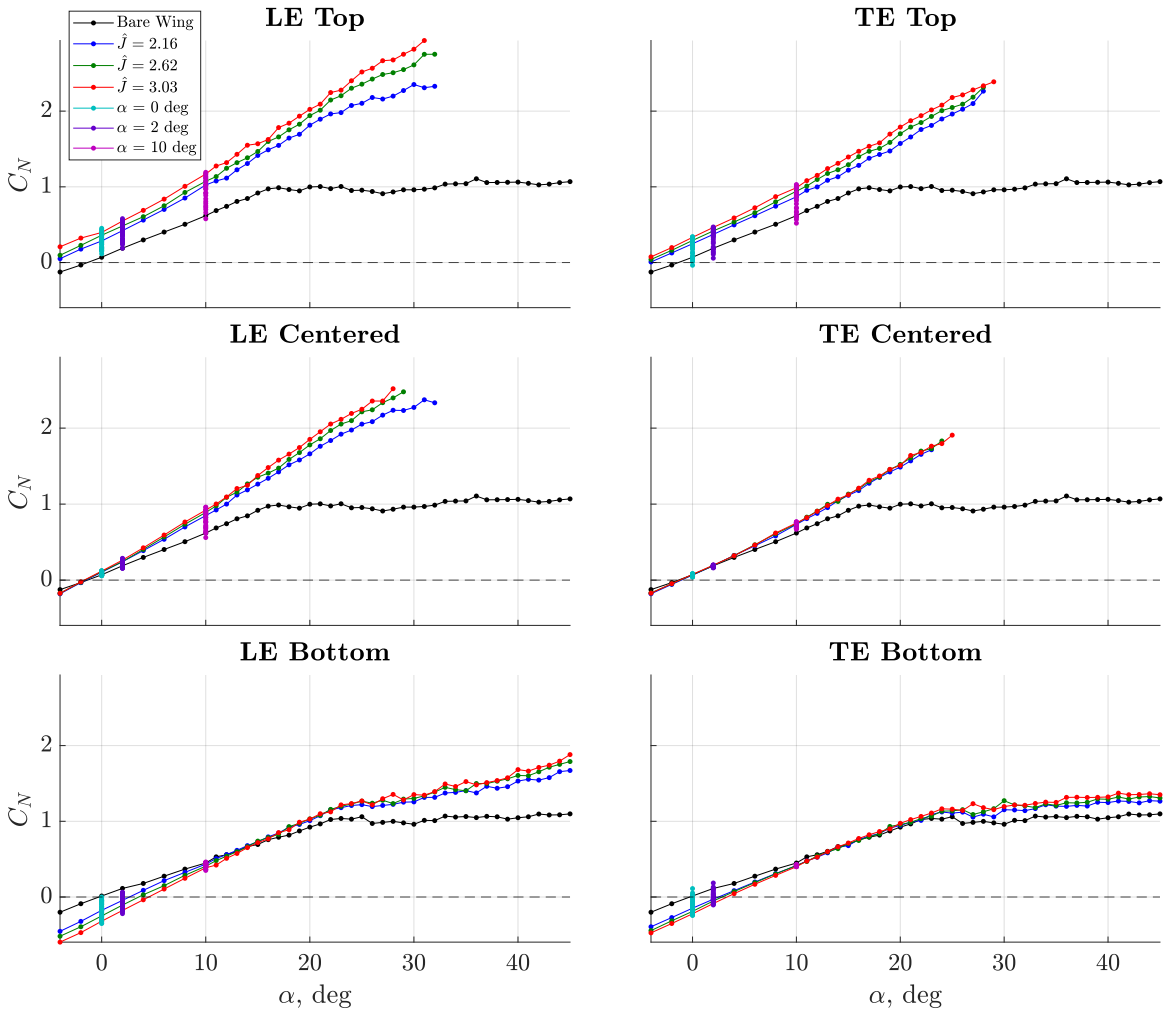


Fig. 13 C_N effect of fan speed across angle of attack for $5F$ configurations.

Question 4 is addressed next to study how the fan position affects C_N across angle of attack. Figure 14 displays all of the combinations of the constant n_F and $\hat{J}$ factors across angle of attack for each F_{pos} configuration, and Fig. 15 more clearly conveys the associated delta effect compared to the respective Bare Wing configuration, with the same insights gleaned from both sets of visualizations. For the $1F$ cases, the F_{pos} effect is subtle across low- to mid-angle of attack, with only a slight increase seen for the Top and a slight decrease for the Bottom and Centered configurations, regardless of the throttle setting. For the $3F$ and $5F$ cases, the F_{pos} effect becomes more apparent. The blown-wing LE Top configuration provides the strongest aeropropulsive interaction effect, resulting in a large increase in C_N across all angles of attack. Although smaller than the blown-wing effect, the suction effect seen for the TE Top configuration still provides a significant increase in C_N with a similar trend to the LE Top case. The Centered configurations show little effect at low angles of attack compared to the Bare Wing, with a larger slope for the LE Centered position resulting in a larger increase in C_N across higher angles of attack compared to the TE Centered position. The LE and TE Bottom

configurations both produce a reduction in C_N up until an angle of attack of 10 deg, no effect at mid-angles of attack, and then an increase in normal force at higher angles of attack. Unlike for the Top and Centered positions, the measured normal force drops off at high angles of attack in all conditions tested for these cases. The magnitudes of the effects are generally larger for the LE compared to the TE, and increase with higher n_F and $\hat{J}$.

Because it is understood that C_L is more traditionally referred to when considering wing or vehicle aerodynamics, the results in Fig. 14 are also shown for C_L in Fig. 16. Most noticeably, additional lift production is observed here due to the component of thrust pointing in the vertical direction. Furthermore, the LE Centered results lie consistently below the TE Top results for the $5F$ cases.

With these results in mind, if maximum normal force is essential either for augmented lift or roll control, positioning the fans at the LE Top would be recommended, and the TE Top would also be acceptable. For minimal effect on C_N due to a change in throttle setting across the low- to mid-angle-of-attack range, the DEP array could be placed at the TE Centered position, or secondarily at the LE Centered position. LE and TE Bottom positions may be considered for minimizing the aeropropulsive interactions for a vehicle operating at mid- to high angle of attack, but caution should be used considering the inefficiencies associated with the lift reduction at low angle of attack.

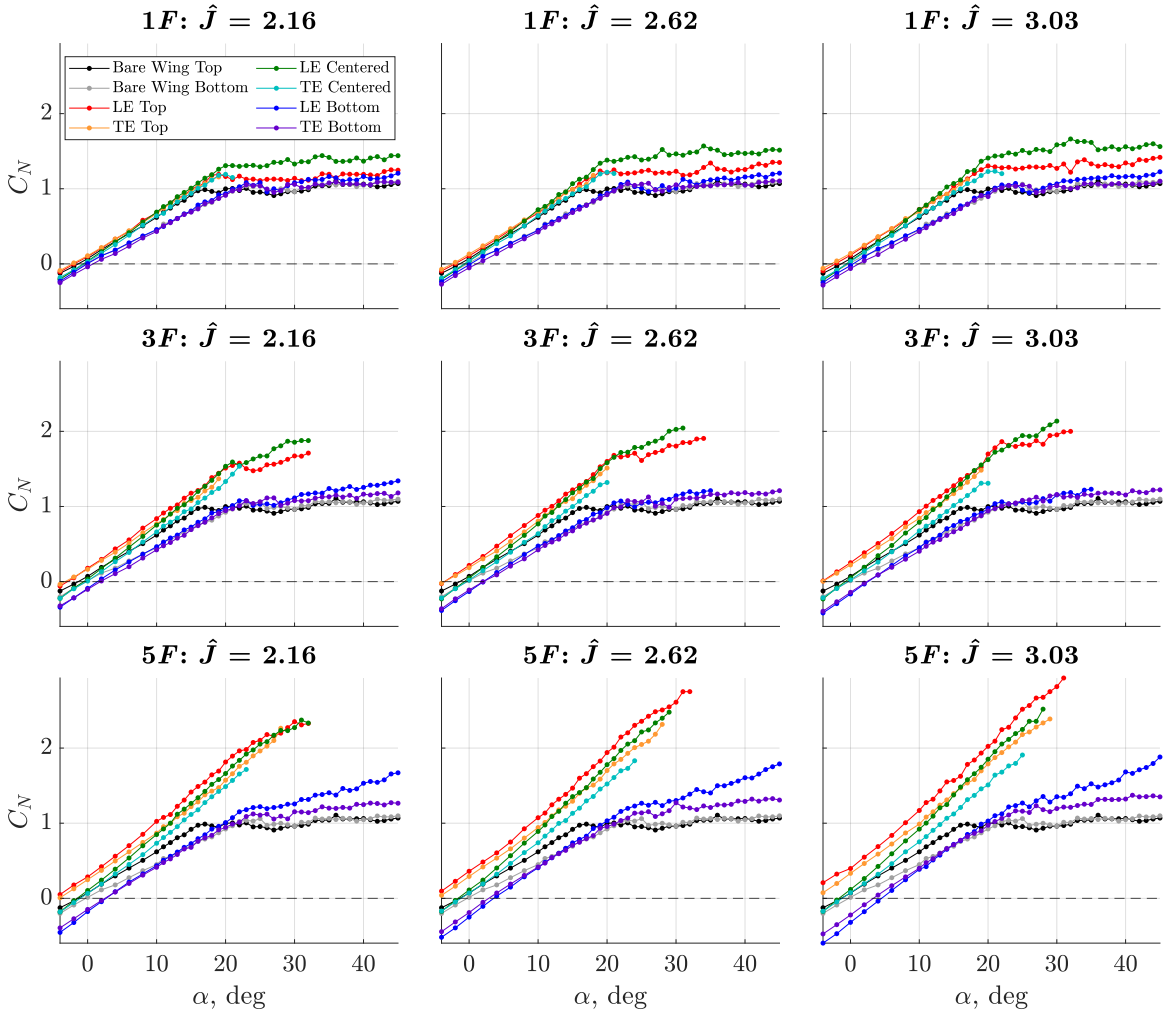


Fig. 14 C_N effect of F_{pos} across angle of attack for all combinations of $\hat{J}$ and n_F.

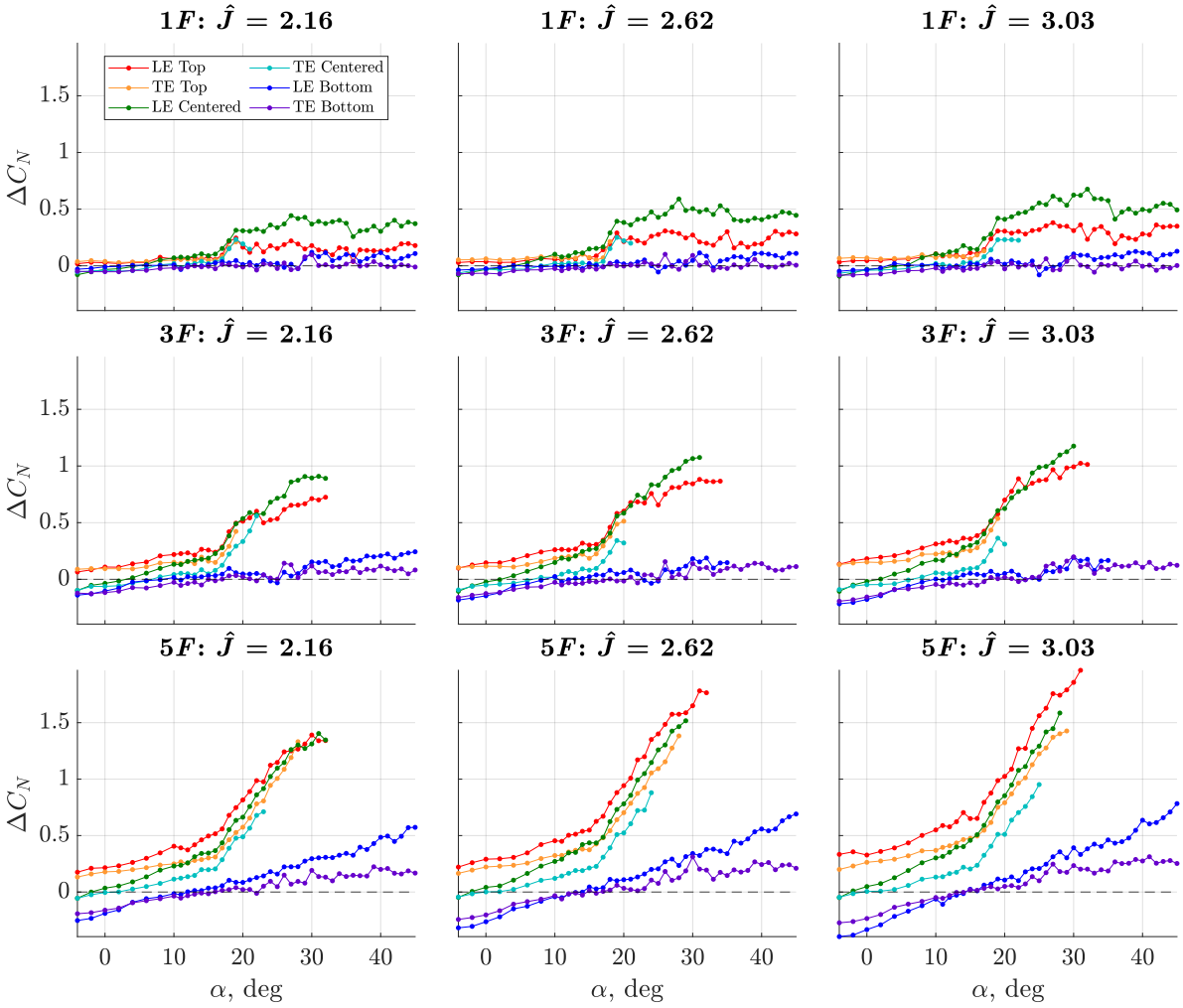


Fig. 15 ΔC_N effect of F_{pos} across angle of attack for all combinations of $\hat{J}$ and n_F.

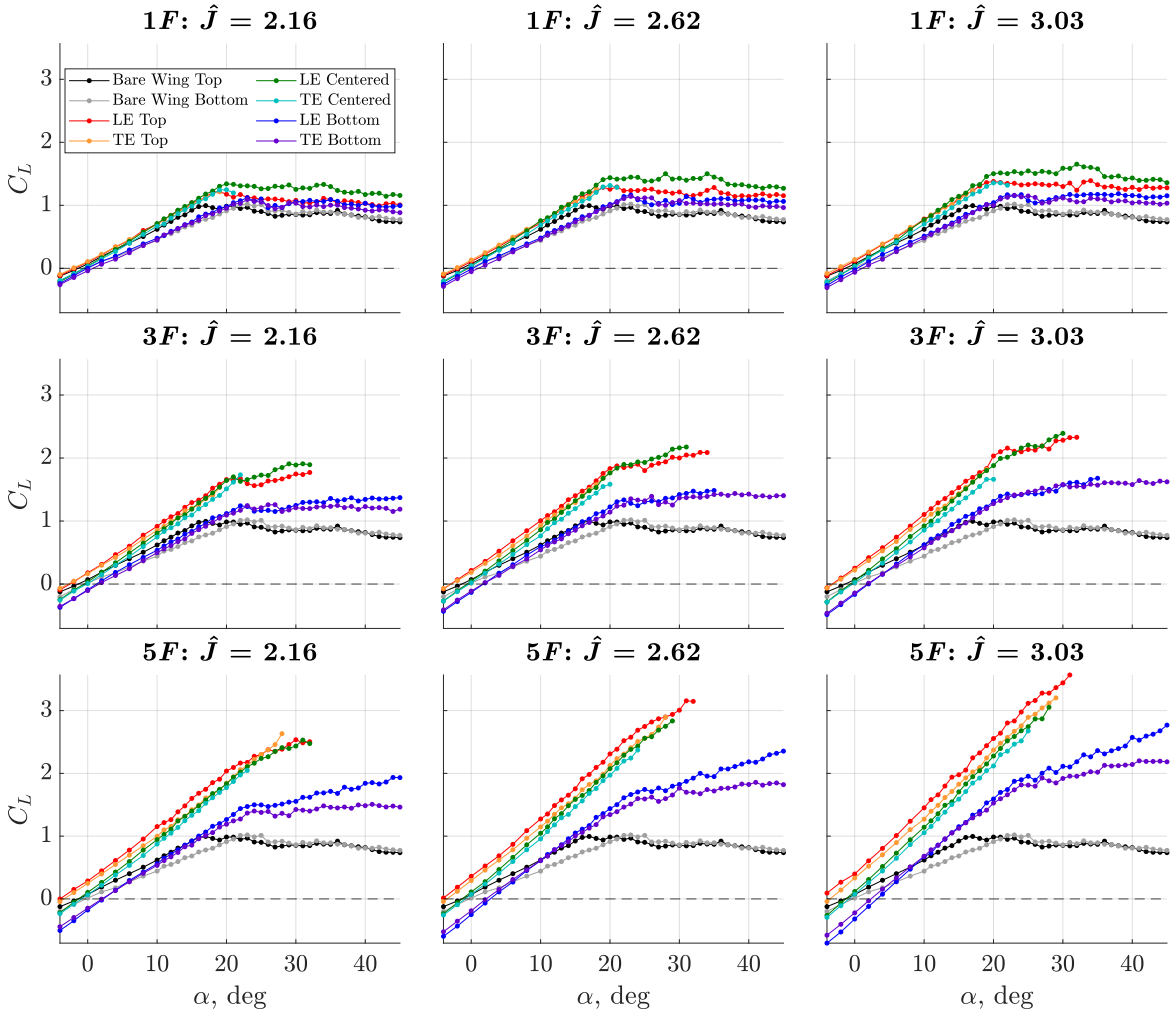


Fig. 16 C_L effect of F_{pos} across angle of attack for all combinations of $\hat{J}$ and n_F.

The final set of normal force results addresses Questions 5 and 6 relating to the aeropropulsive effect on C_{N_α}, which is defined as $C_{N_\alpha} = \partial C_N / \partial \alpha$, and was computed numerically using central differencing for the interior data points and with single-sided differencing for the endpoints. The other gradients discussed throughout this paper were computed in the same manner. Figure 17 displays the C_{N_α} results corresponding to those shown in Fig. 14 up to an angle of attack of 16 deg. Compared to the Bare Wing, all of the F_{pos} generally produce a larger C_{N_α}. Relative to the Bare Wing Top results, the largest magnitude change is seen for the LE Centered position across n_F and $\hat{J}$, and the smallest magnitude change is shown for the TE Top and TE Centered cases. Relative to the Bare Wing Bottom results, a larger change is seen for the LE Bottom compared to the TE Bottom configuration. These insights are consistent with what was seen and discussed in Fig. 11, with a larger magnitude slope generally noted for the LE compared to the TE positions. The slopes remain fairly constant across the linear angle-of-attack range, with small increases seen for some configurations.

The effect of n_F on the normal force slope is considered last. Figure 17 indicates a small increase in slope as n_F

increases, but this effect is dependent upon angle of attack. Referring to Fig. 11, the TE Centered position, for example, shows no C_{N_α} change at low angles of attack, regardless of n_F. Conversely, a notable effect is seen at higher angles of attack. The n_F effect on C_{N_α} is generally stronger for the LE positions than for the TE positions.

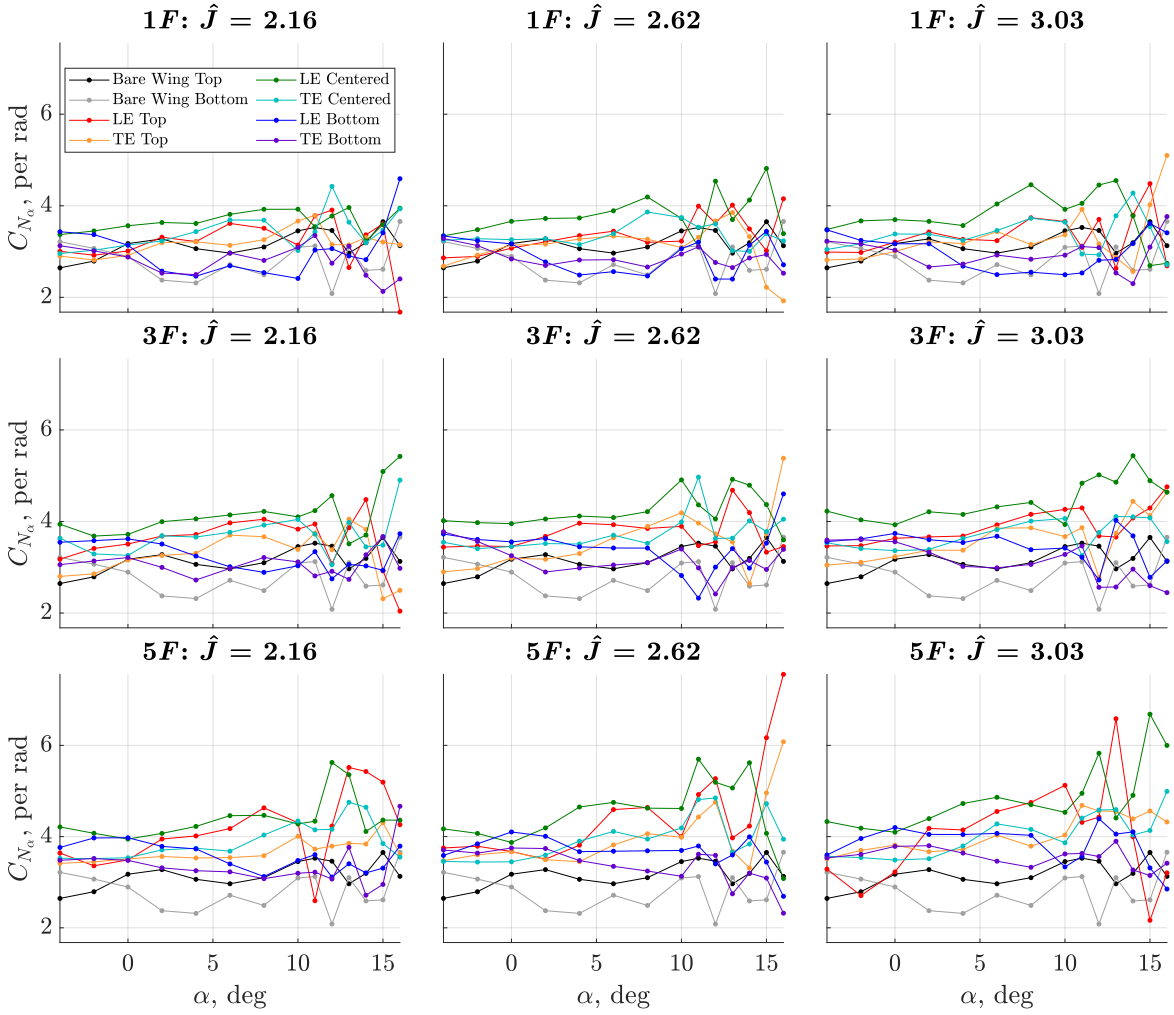


Fig. 17 C_{N_α} effect of F_{pos} across angle of attack for all combinations of $\hat{J}$ and n_F.

B. x-Force Coefficient

The body-axis x-force coefficient data were analyzed in a different manner from the normal force coefficient data to focus on the variations in thrust produced from the DEP array between F_{pos} and the angle-of-attack and fan speed factors. Because only a single balance was used throughout the test to measure the total aerodynamic and propulsive forces and moments, the C_X measurements shown and discussed include contributions from both the fan thrust and the model drag, which is dependent upon the fan array placement on the wing. As a result, insights gleaned and conclusions drawn may not be independently driven by relative thrust performance. If separate balances had been used to measure the thrust and aerodynamic contributions, then the individual effects could have been more easily distinguished.

There are five research questions that are addressed with the C_X results:

7) Do the aeropropulsive effects on C_X vary linearly with increasing n_F (Fig. 18)?

8) How do F_{pos} and $\hat{J}$ affect the linearity of the aeropropulsive effects on C_X with increasing n_F (Fig. 19)?

9) How does $\hat{J}$ affect the $1F$ linear extrapolation (Fig. 20)?

10) How do the aeropropulsive effects on C_X vary between F_{pos} (Fig. 21)?

11) How do the aeropropulsive effects on C_X compare to a prediction based upon the superposition of Bare Wing aerodynamics and fan propulsive effects (Fig. 21)?

In an analogous manner to C_N, Question 7 is addressed in Fig. 18 for the results with $\hat{J} = 3.03$ to investigate the aeropropulsive extrapolation of the $3F$ and $5F$ cases compared to one another and to the $1F$ results. Relative to the $1F$ prediction across the low- to mid-angle-of-attack range, an adverse interaction effect is apparent for the TE Top, LE Centered, LE Bottom, and TE Bottom configurations, with the $1F$ extrapolation improving from $3F$ to $5F$ and across angle of attack for the TE Centered position. However, although not shown in these results, the lower fan speed sweeps displayed a more clearly penalizing array effect for the TE Centered configuration compared to the $1F$ prediction. In other words, for those configurations, $3\times$ and $5\times$ the thrust produced in the $1F$ configuration compared to the baseline wing would result in more than what was measured, implying a collective reduction in thrust produced by the array. This is consistent with the adverse effect noted in the static results in Fig. 10 and is understood as a finite amount of spatial airflow shared across the array. The LE Top results align well with the $1F$ extrapolation, indicating no notable loss in fan efficiency due to the effect of the array. The $3F$ to $5F$ extrapolation is also satisfactory for the LE Top, TE Top, and LE Centered configurations, with the TE Centered, LE Bottom, and TE Bottom results showing a poorer extrapolation. However, whereas this extrapolation is consistent across the other fan speed setpoints for the LE Centered and TE Bottom configurations, the quality of the extrapolation for the other positions varied between fan speeds, so this assessment is generally inconclusive for those cases. In general, the $3F$ to $5F$ extrapolation is closer than the $1F$ extrapolation.

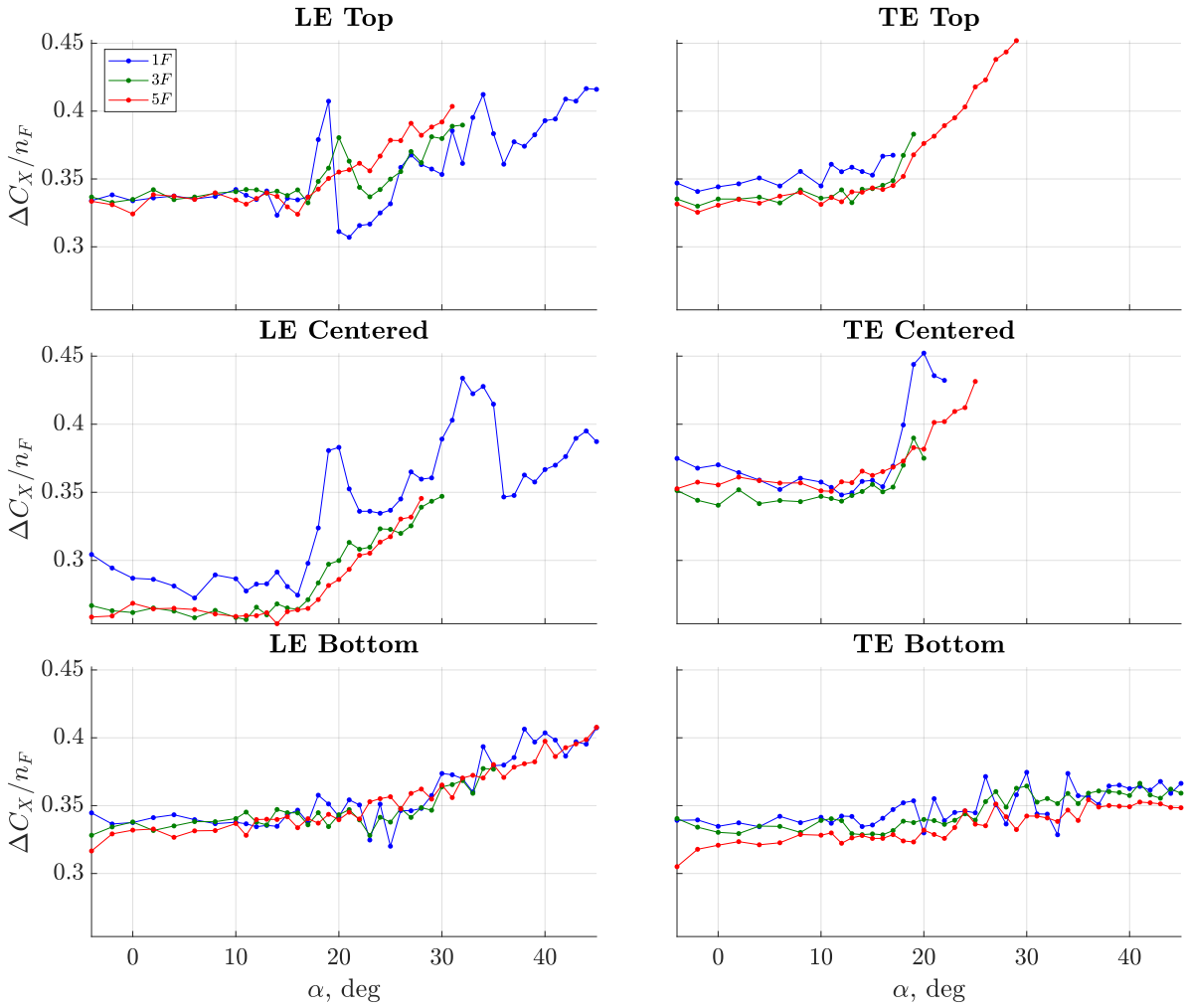


Fig. 18 C_X aeropropulsive extrapolation effect across angle of attack at $\hat{J}$ = 3.03.

Question 8 is addressed in Fig. 19, which displays the n_F aeropropulsive extrapolation in another way to discern the effects of $\hat{J}$ and F_{pos}. In this visualization, the ΔC_X results are normalized by the results from the $1F$ configuration $\Delta C_{X_{1F}}$, to display quantitatively and more clearly how close to 3× and 5× the $1F$ prediction lies. The LE Top position produces the largest magnitude of ΔC_X relative to the $1F$ linear prediction, with some cases even exceeding the linear expectations, particularly at lower $\hat{J}$. In addition to producing the least thrust due to the wing blockage, as seen in the static results in Fig. 9, the LE Centered position also produces the poorest propulsive interaction effect for the array. The linear extrapolations generally improve as $\hat{J}$ increases, with better results seen across F_{pos} for $3F$ than for $5F$.

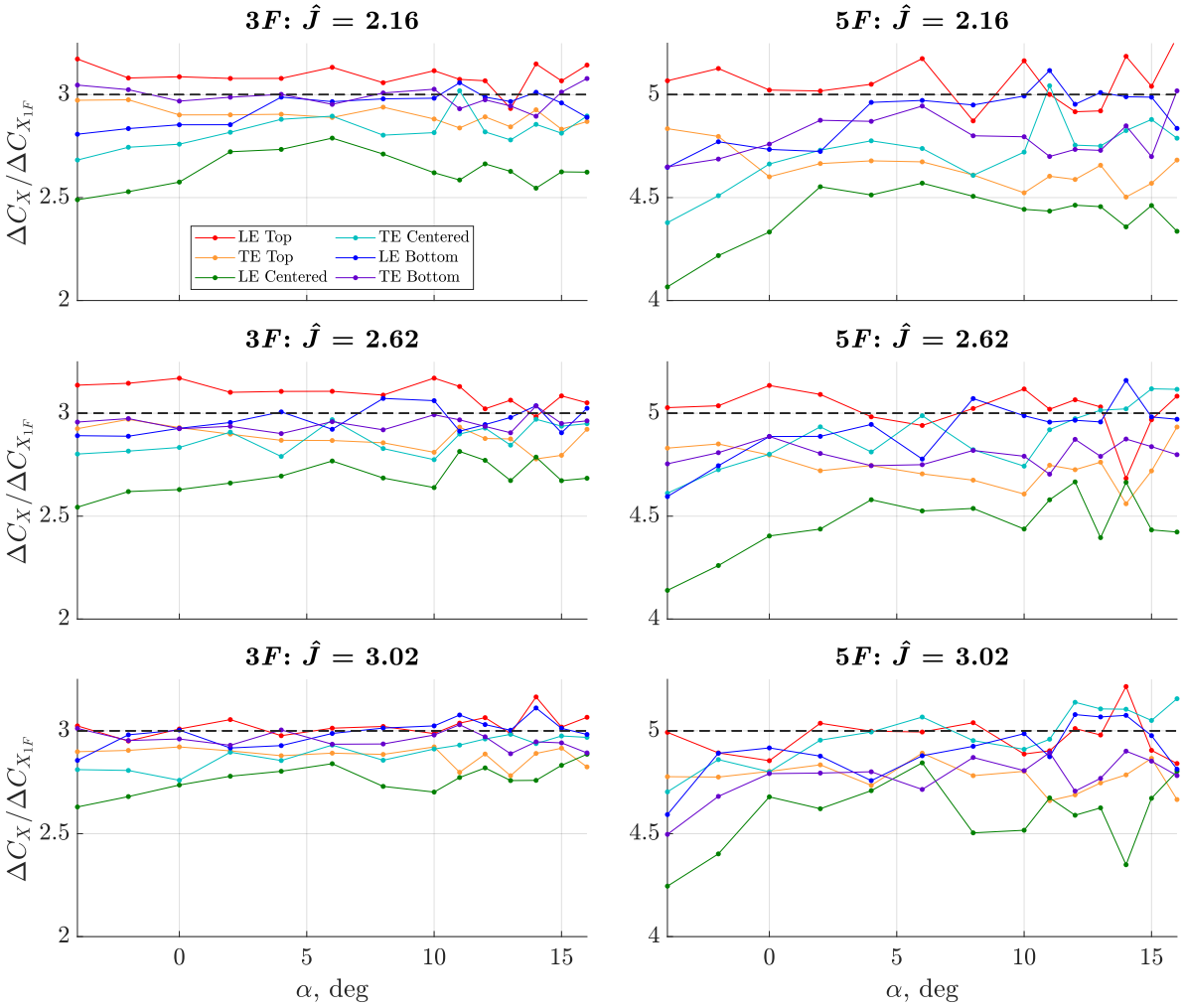


Fig. 19 C_X aeropropulsive $1F$ extrapolation effect for $3F$ and $5F$ configurations.

Question 9 assesses the linear extrapolation effect across fan speed and is addressed in Fig. 20 across the relevant throttle range corresponding to a minimum of PWM = 1375 μs, as described in Fig. 9. In this visualization, the ΔC_X results are normalized by both n_F to remove the 3× and 5× effects, and by $\Delta C_{X_{1F}}$ to relate the data to that which is seen from the $1F$ case, with the results providing additional insight beyond what is distinguishable in Figs. 18 and 19. Reflecting the inconclusive nature of the $3F$ to $5F$ extrapolation for many configurations, as discussed in Question 7, there are some notable differences between the $3F$ and $5F$ results across $\hat{J}$ seen here. The LE Top position exhibits a close-to-linear result across the full throttle range shown, whereas the TE Top position shows a constant result across $\hat{J}$ that is less than a $1F$ linear extrapolation. The LE and TE Bottom positions show a similar overprediction effect as the TE Top position but at a smaller magnitude. For the LE Centered and TE Centered positions, the $1F$ linear extrapolation improves as $\hat{J}$ increases, with a more favorable result shown for the TE Centered compared to the LE Centered position. To summarize, increasing fan speed does not affect the $1F$ linear prediction for the Top and Bottom

cases, and the prediction improves across increasing fan speed for the Centered positions.

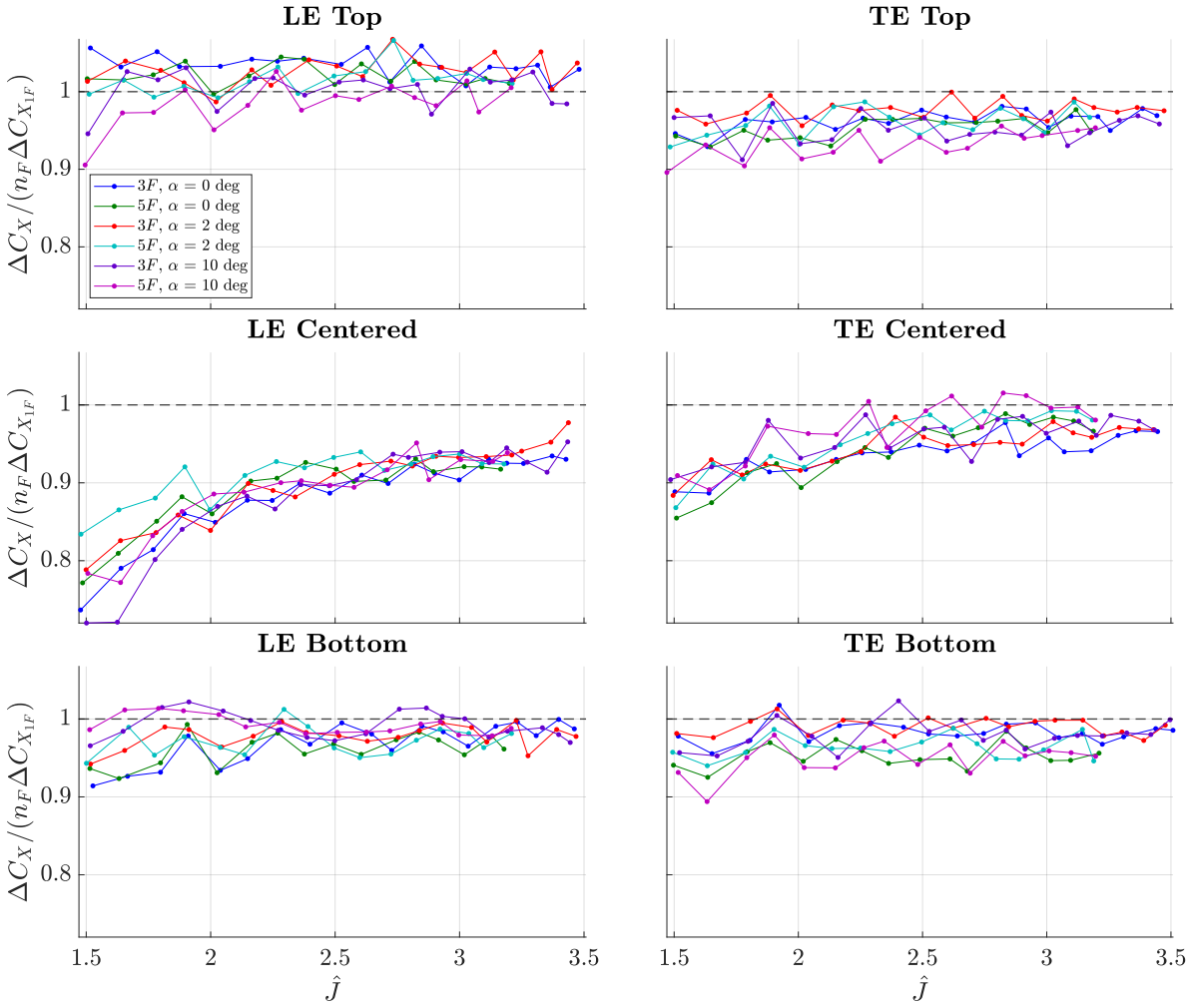


Fig. 20 C_X effect of fan speed on the aeropropulsive $1F$ extrapolation effect.

Finally, Questions 10 and 11 are explored in Fig. 21, which shows the effect of F_{pos} across angle of attack for each of the n_F and $\hat{J}$ combinations. The ΔC_X effect is shown here to compare the Top and Bottom configurations directly to one another, each of which is plotted relative to the respective Bare Wing aerodynamics. Note that the scale was adjusted for each set of n_F plots to more clearly distinguish comparative features. A fan speed effect can be seen across the sets of plots for each throttle setpoint that generally shifts the plots upward without changing the shape, due to the associated thrust increase. The TE Centered position produces the result with the largest thrust and/or least drag as measured with C_X. Note that this could be in part due to a BLI effect based upon the position of the fans behind the wing and the resulting reduction in drag when the wake is ingested by the fans, which would indicate an improved operational efficiency [22]. However, a distinction between thrust and drag contributions to C_X is not achievable given the limitations of the test setup with a single balance measuring the combined aerodynamic and propulsive effects.

Nevertheless, the net effect is still seen as promoting a TE Centered fan position for improved net thrust and overall efficiency. As was reflected in the static results, the LE Centered position produces significantly less thrust/more drag as compared to the other fan positions due to the wing blockage directly behind the fan efflux; this effect becomes more apparent at higher $\hat{J}$ and n_F. A pylon effect resulting in increased drag may also be apparent for this case. The Top and Bottom configurations generally produce comparable results for C_X, with the LE and TE alignment across low- to mid-angles of attack improving across n_F for the Top positions and degrading slightly for the Bottom positions. Altogether, there is very little effect between the Top and Bottom positions for most cases.

Using these results as guidance, for maximum thrust/minimal drag and maximum yaw control considerations, fan placement at the TE Centered position is recommended, followed by the Top and Bottom positions, whereas there is vastly reduced performance and effectiveness at the LE Centered position.

Question 11 considers a prediction based upon the isolated EDF characterization results in Ref. [16] to understand if a superposition of aerodynamic and propulsive effects is valid in any cases. Considering the close alignment of the Top and Bottom results, the isolated fan effect matches well with all of these cases across n_F and $\hat{J}$, but tends to lie on the upper end of this collection of data, indicating a slight penalty due to the aeropropulsive effect. A BLI effect considered for the TE Centered position is reinforced with this insight, as those results consistently perform better than the isolated fan prediction, indicating a favorable effect for that fan placement, despite any penalizing array effects.

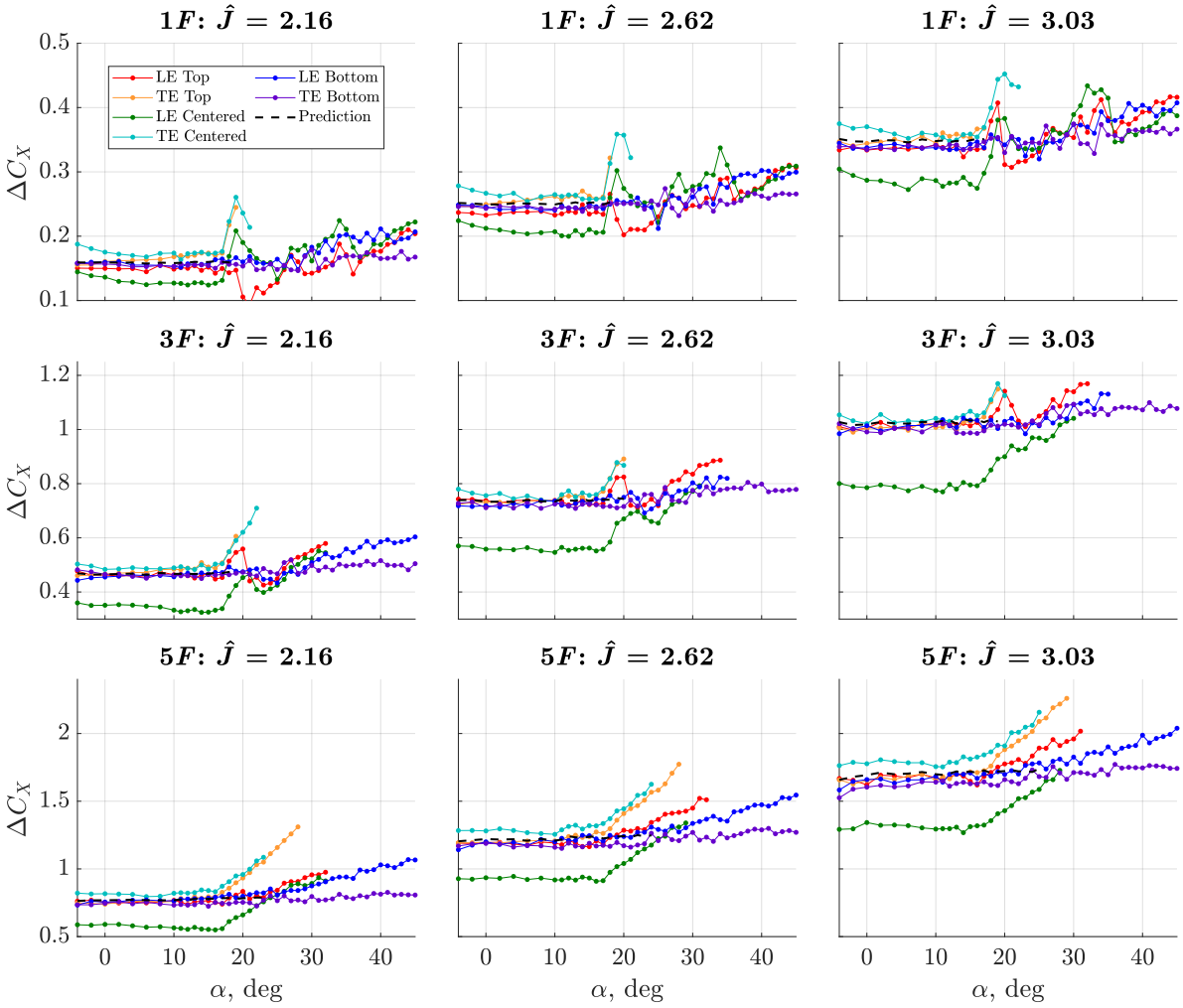


Fig. 21 ΔC_X effect of F_{pos} across angle of attack for all combinations of $\hat{J}$ and n_F.

C. Pitching Moment Coefficient

The pitching moment coefficient consists of an aerodynamic component based upon the fan-mounted wing configuration, as well as a propulsive contribution from the applied thrust vector with the moment reference center positioned at the center of the internal ribs. The pitching moment results, analysis, and insights are strongly dependent upon the center of gravity (CG) for a particular integrated vehicle design, so if the CG is above or below the wing, the aeropropulsive characteristics discussed in this section may not be applicable.

The C_m results are analyzed through a series of research questions that are summarized as follows:

12) Do the aeropropulsive effects on C_m vary linearly with increasing n_F (Fig. 22)?

13) How does $\hat{J}$ affect C_m (Fig. 23)?

14) How do n_F and angle of attack setpoint affect C_m across $\hat{J}$ (Fig. 23)?

15) How do the aeropropulsive effects on C_m vary between F_{pos} (Fig. 24)?

16) How do the aeropropulsive effects on C_{m_α} vary between F_{pos} (Fig. 25)?

17) How do the aeropropulsive effects on C_m compare to a prediction based upon the superposition of Bare Wing aerodynamics and fan propulsive effects (Fig. 24)?

18) How do the aeropropulsive effects on $C_{m_{\hat{J}}}$ vary between F_{pos} (Fig. 26)?

Question 12 considers the linearity assessment of the pitching moment results across n_F, and is analyzed in the same manner as for C_N and C_X, with the results shown in Fig. 22 for $\hat{J} = 3.03$. Note that different scales are used for the Top, Centered, and Bottom configurations. The $1F$ extrapolation results underpredict the magnitude of C_m for the LE Top and LE Bottom configurations, and conversely, they overpredict the measurements for the TE Top and TE Bottom positions. That is to say, the DEP array effect on C_m is amplified at the LE and mitigated at the TE for the Top and Bottom positions. The $1F$ extrapolation for the Centered positions seems to improve at higher n_F, with an excellent fit seen for the TE Centered position and a relatively poor fit for the LE Centered position. Despite these observations, the $1F$ extrapolation results are generally considered inconclusive for most configurations due to the variability in trends across the $\hat{J}$ setpoints. The Top and Bottom configurations showed excellent linearity between the 3× and 5× arrays, with the Centered positions showing poor extrapolation.

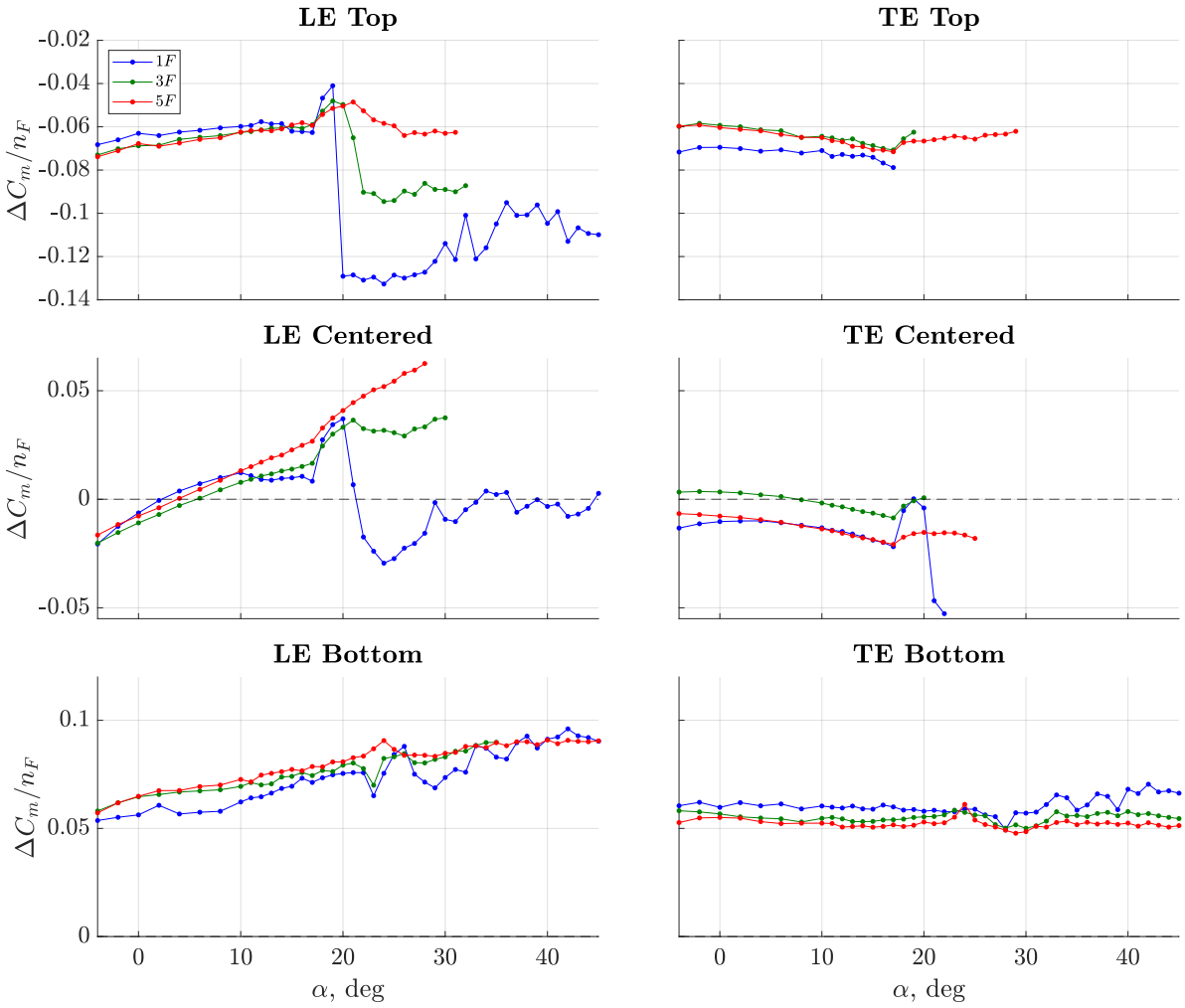


Fig. 22 C_m aeropropulsive extrapolation effect across angle of attack at $\hat{J}$ = 3.03.

Questions 13 and 14 are addressed in Fig. 23, which displays the pitching moment results across $\hat{J}$ for all of the n_F and angle-of-attack setpoints. Note that the plot scales are different for the Top, Centered, and Bottom positions here as well to more clearly discern distinguishing features. As $\hat{J}$ is increased, an increasing negative C_m is apparent for the Top, and an increasing positive C_m for the Bottom positions. For both of these sets of configurations, n_F increases the magnitude of the pitching moment; when these results were normalized by n_F, the plots generally lined up closely to one another, in congruence with the nearly linear relationship discussed previously for most configurations. The LE Top and LE Bottom positions show an increasing C_m with angle of attack for each clustered collection of n_F cases, indicating an unstable pitching moment curve across 0 to 10 deg angle of attack, whereas the TE Top position shows the opposite relationship, suggesting a stabilizing pitching moment. The TE Bottom case shows only a small change across angle of attack, which suggests a flat pitching moment curve.

For the LE and TE Centered positions, the centers of the fans in the array were aligned closely with the moment

reference center, thus mitigating the thrust contribution to the pitching moment results. For the LE Centered position, there is no notable $\hat{J}$ effect aside from a small increase in C_m across $\hat{J}$ for the $5F$ configuration at an angle of attack of 10 deg, indicating a destabilizing effect at higher angles of attack. For the TE Centered position, there is a small decrease in C_m for all of the $5F$ configurations, suggesting a stabilizing effect may be present in this case at higher n_F and angles of attack.

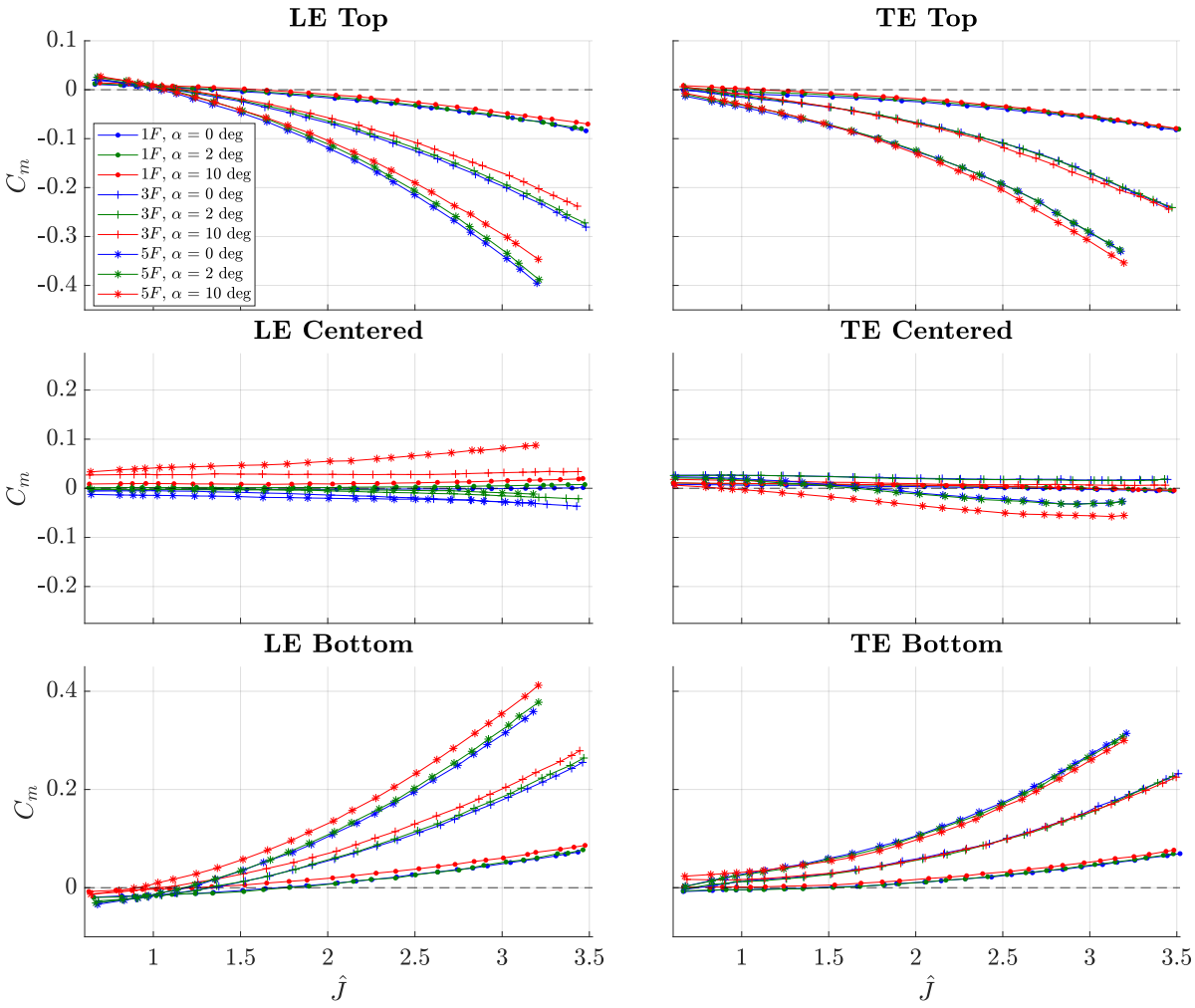


Fig. 23 C_m effect of n_F and angle of attack setpoint across $\hat{J}$.

For Questions 15 and 16, the effect of F_{pos} on C_m is displayed across angle of attack in Fig. 24 for each combination of n_F and $\hat{J}$ setpoints. Figure 25 displays the associated C_{m_α} results up to 16 deg and can be analyzed in parallel to provide a deeper understanding of the fan effects on longitudinal static stability. For the $1F$ cases in Fig. 25, there are no notable changes in C_{m_α} from the nearly flat curve seen for the Bare Wing other than for the LE Centered position; rather, in Fig. 24, as $\hat{J}$ is increased, the results for the Top and Bottom configurations shift away from zero in the negative and positive directions, respectively, and the results from the Centered positions remain well-aligned with the Bare Wing.

As n_F increases to $3F$ and $5F$, there are several features to note. In addition to corresponding changes in the magnitude of C_m with increasing n_F and $\hat{J}$ as noted previously, a moderately destabilizing slope change becomes increasingly apparent for the LE Top and LE Bottom positions; a small stabilizing slope change is seen for the TE Top and TE Centered positions, with a slight effect for the TE Bottom position; and a substantial destabilizing effect is seen for the LE Centered position. All of these effects, particularly for the LE Centered position, are less apparent for $3F$, whereas they deviate more from the Bare Wing results at $5F$.

A strong sensitivity of the pitching moment results to increasing n_F, but not to increasing $\hat{J}$, is seen for the LE Centered position. This was determined to be the effect of the freestream velocity impinging on the pylons shown in Fig. 3d and causing separated flow across the bottom of the wing, and/or the effect of the aerodynamic force on the pylon. This was seen to induce a destabilizing pitching moment as angle of attack was increased and the impact of the pylons correspondingly became larger. For the TE Centered position, the effect was conversely stabilizing. This indicates that while the Top and Bottom configurations were mounted in comparable manners, a direct comparison to the Centered configurations may be affected by the pylon design. The pylon was designed to configure the fans along the chord line using the existing hardware that would integrate into the rig; however, a more streamlined design may be considered for a more direct comparison to the other fan positions. Nevertheless, the results would still be dependent on that particular pylon design and integration.

For design considerations that prioritize static stability provided by DEP, the TE Centered position appears to offer the most favorable stabilizing effects, followed by the TE Top and then the TE Bottom position, whereas the LE Centered, LE Top, and LE Bottom positions provide a destabilizing pitching moment.

To address Question 17, the isolated EDF characterization results from Ref. [16], along with the distance between the fans and the moment reference center, which was placed at the center of the rig, were used to predict the pitching moment coefficient results for the Top and Bottom configurations, as shown together with the measured results in Fig. 24. For the $1F$ cases, only small differences are seen between the LE and TE Top, and between the LE and TE Bottom configurations, and the prediction aligns well with each of these, even as $\hat{J}$ increases. As n_F increases to $3F$, the prediction degrades for the Top configurations as $\hat{J}$ increases and the results move apart. The LE and TE Bottom results deviate more strongly from one another, with the prediction matching the overall magnitude, although not the slope, for the LE Bottom case. As n_F increases to five, the stabilizing or destabilizing effects seen in many of the F_{pos} results are not reflected in the prediction, which remains mostly flat, similar to the Bare Wing. For the Top configurations at $\hat{J} = 2.16$, the prediction still aligns well with the LE Top results but degrades as $\hat{J}$ increases, and lies between the LE and TE Top results for $\hat{J} = 3.03$. The alignment to the LE Bottom configuration continues to degrade as the destabilization effect becomes stronger.

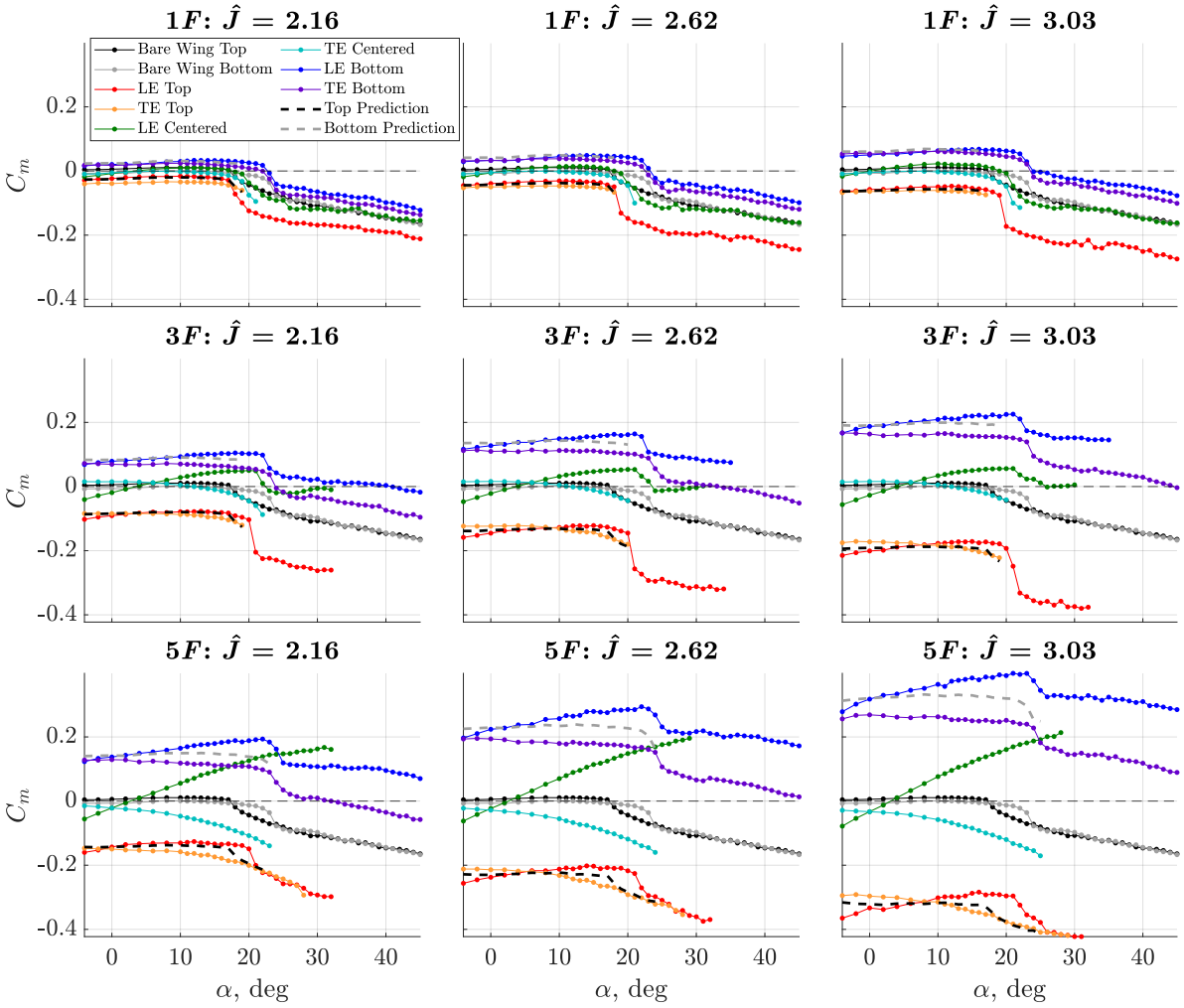


Fig. 24 C_m effect of F_{pos} across angle of attack for all combinations of $\hat{J}$ and n_F.

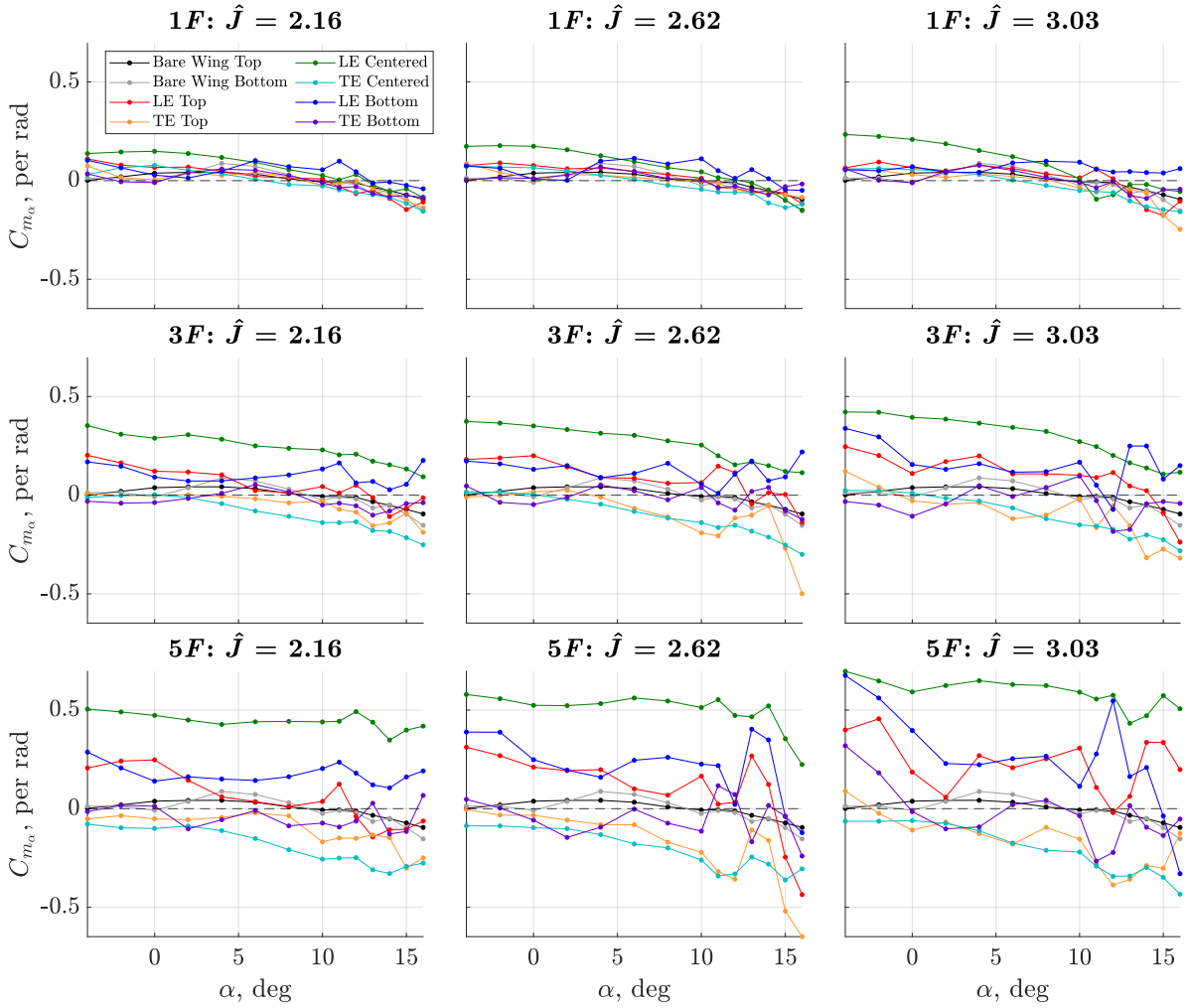


Fig. 25 C_{m_α} effect of F_{pos} across angle of attack for all combinations of $\hat{J}$ and n_F.

Question 18 considers that in addition to adjustments in vehicle speed, lift, yawing moment, and rolling moment, fan speed may also be varied to change the pitching moment, particularly when the fans are placed on the Top and Bottom surfaces for a moment reference center at the center of the wing. Figure 26 displays the absolute value of C_{m_j} across $\hat{J}$ for each of the fan positions at the discrete angle-of-attack setpoints and n_F. A stronger effectiveness is generally seen for fan speed adjustments at high throttle compared to low throttle, indicating a nonlinear effect that is also apparent in Fig. 23. At low angles of attack, the strongest pitching moment effect is seen for the LE Top and LE Bottom positions, with a slightly weaker effect apparent for the TE Top and TE Bottom configurations. At an angle of attack of 10 deg, these LE and TE results do not align as closely, with the LE Bottom position producing the strongest effect and the TE Bottom position resulting in the weakest effect. The LE and TE Centered positions have a small and mostly constant $|C_{m_j}|$ effect across $\hat{J}$, with the TE Centered position showing slightly higher effectiveness for the $5F$ cases.

Fan speed setting introduces an additional control effector for the flight vehicle that could be used for pitch control

and potentially enable additional vehicle trim states. However, this effect may also not be a desirable function of DEP; rather, the horizontal tail may be used to retrim the vehicle and remove the pitching moment effect due to fan speed. Control approaches that leverage the aeropropulsive benefits must therefore account for pitching moment while using the DEP for thrust, yaw, lift, and/or roll adjustments.

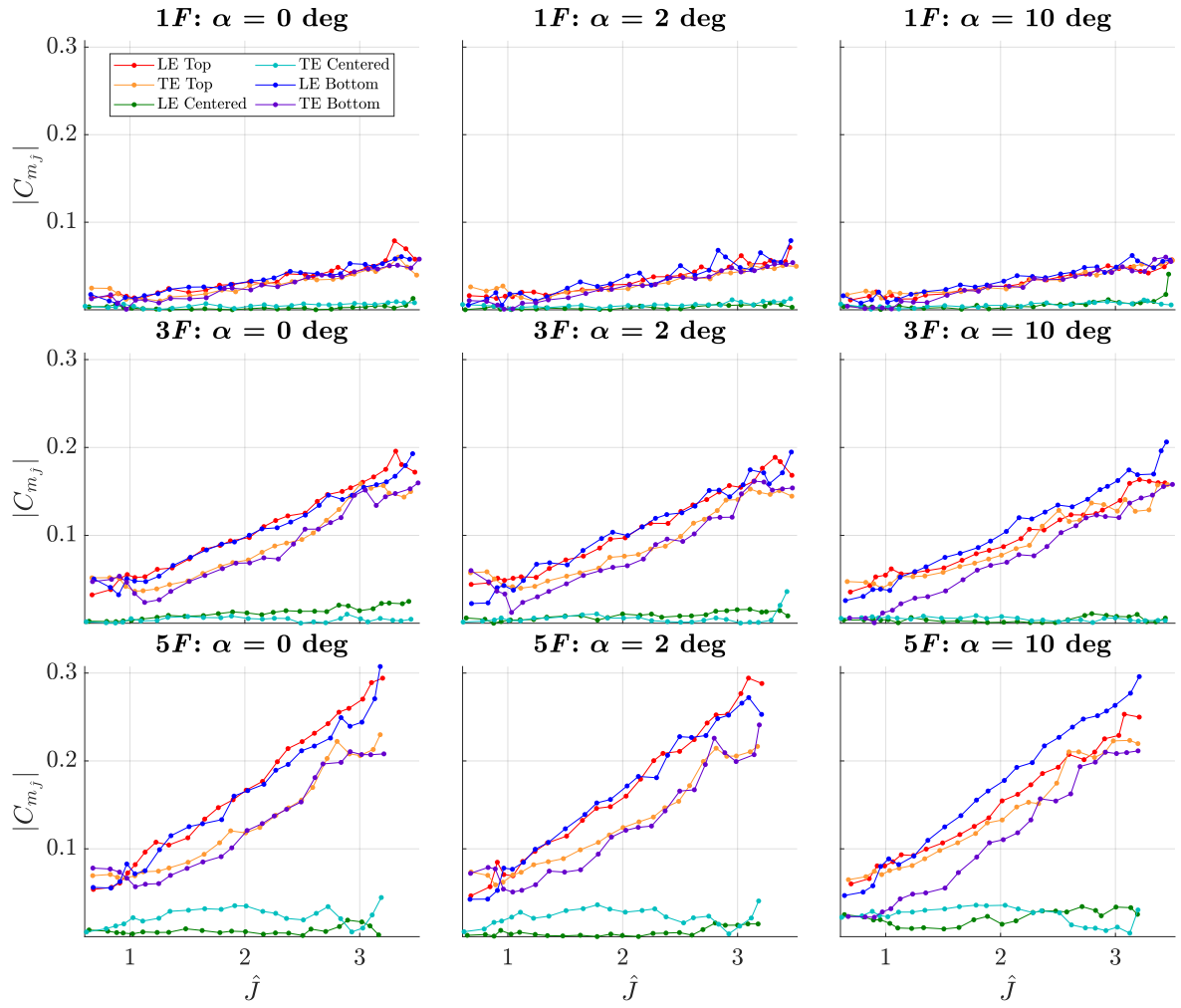


Fig. 26 C_{m_j} effect of F_{pos} across $\hat{J}$ for all combinations of angle of attack setpoint and n_F.

D. Summary of Aeropropulsive Results

The C_N, C_X, and C_m aeropropulsive effects resulting from DEP integration into the ADEPT Wing were presented in the previous subsections, and factors varied included angle of attack and uniform fan speed, as well as n_F and F_{pos}. This subsection summarizes in Tables 5–7 the main effects observed and discussed for each force and moment coefficient across the various considerations. The respective figures that were used to derive those inferences are referenced at the top of each column. An inconclusive field indicates inconsistent trends across $\hat{J}$ for the extrapolation effects.

A relative comparison of fan positions across several key considerations presented in Table 8 for low- to mid-angles

of attack may be useful to offer insight for fan position selection for potential DEP application. A ranking of 1–6 is given to each fan position to describe the relative performance of each configuration across considerations of lift and roll control, thrust and yaw control, static stability, and pitch control. If augmented lift and roll control are a high priority, then the LE Top configuration provides the most favorable result, followed by the TE Top, and so on. If thrust and yaw control are preferable, then the TE Centered configuration may be selected. If wing static stability is important, then the TE Centered or TE Top configurations are recommended. For maximum pitch control, the LE Top or LE Bottom configuration is suggested. Alternatively, for a given fan position, the relative ranking provided in each row can offer insight into the expected performance across each consideration. If only small differences are noted, an apparent tie is indicated with the same number. Note that the pitching moment results are based upon a moment reference center placed at the center of the rig, and the static stability insights for the LE Centered configuration are questionable due to the pylon effect and may be dependent on particular integration designs. Additionally, the pitch control consideration is ranked by the increasing effect of $\hat{J}$ on C_m, but it may be desirable to minimize C_{m_j}, so the opposite ranking could be preferable.

Table 8 also conveys that the integration of DEP into a vehicle induces highly coupled aeropropulsive effects across all of the longitudinal forces and moments. For a given increase in fan speed to increase vehicle airspeed, for example, corresponding changes in all of the longitudinal forces and moments may be apparent. This must be accounted for in a control allocation approach to produce the desired effects.

The results summarized in this subsection and shown throughout the paper are based upon the particular ADEPT Wing design and fan integration, as well as the specific test conditions. As a result, the associated insights and conclusions are limited in scope and may not be generalizable to a broad array of various applications. For example, these test results were obtained for low-speed, incompressible flow conditions, such as near takeoff and landing (which are critical phases of flight where control authority is important), but are not applicable to transonic transport aircraft cruise conditions. Additionally, the EDFs were placed inboard around the center of the wing, and wingtip interaction effects were not considered. The EDF diameter-to-wing-chord ratio may also play a role in the resulting aeropropulsive interactions, and this parameter was held constant in this study. Furthermore, all of the EDFs in the array were run uniformly at a given open-loop throttle command, and interactions between fans running at different fan speeds, as well as the relative effects of each fan on the force and moment coefficients based upon the spanwise array position, were not considered in this work. Finally, the pitching moment results may not be valid for a vehicle CG that is above or below the wing.

Table 5 Summary of aeropropulsive effects for C_N

F_{pos}	n_f and $\hat{J}$ (low α) (Figs. 11 and 13)	n_f and $\hat{J}$ (mid α) (Figs. 11 and 13)	n_f and $\hat{J}$ (high α) (Figs. 11 and 13)	$1F$ prediction (Fig. 12)	$3F$ to $5F$ prediction (Fig. 12)
LE Top	+++	+++	+++	Under	Good
TE Top	++	++	++	Over	Good
LE Centered	N/A	++	++	Under	Marginal
TE Centered	N/A	+	+	Under	Marginal
LE Bottom	−−	N/A	++	Over	Good
TE Bottom	−	N/A	+	Under	Good

Table 6 Summary of aeropropulsive effects for C_X

F_{pos}	$1F$ prediction (Figs. 18 and 19)	$3F$ to $5F$ prediction (Fig. 18)	$1F$ prediction across $\hat{J}$ (Fig. 20)
LE Top	Good	Inconclusive	Constant
TE Top	Over	Inconclusive	Constant
LE Centered	Over	Good	Improving
TE Centered	Over	Inconclusive	Improving
LE Bottom	Over	Inconclusive	Constant
TE Bottom	Over	Marginal	Constant

Table 7 Summary of aeropropulsive effects for C_m

F_{pos}	n_F and $\hat{J}$ (Fig. 24)	$1F$ prediction (Fig. 22)	$3F$ to $5F$ prediction (Fig. 22)
LE Top	Negative	Under	Good
TE Top	Negative	Over	Good
LE Centered	Small	Inconclusive	Marginal
TE Centered	Small	Inconclusive	Poor
LE Bottom	Positive	Under	Good
TE Bottom	Positive	Inconclusive	Good

Table 8 Summary of main aeropropulsive effects relating to selection of fan position, with "1" indicating the most favorable and "6" the least favorable position

F_{pos}	Lift & roll control (Figs. 14 and 16)	Thrust & yaw control (Fig. 21)	Static stability (Figs. 24 and 25)	Pitch control (Fig. 26)
LE Top	1	2	4	1
TE Top	2	2	2	3
LE Centered	3	6	6*	6
TE Centered	4	1	1	5
LE Bottom	6	2	5	1
TE Bottom	5	2	3	3

*Inconclusive result

VII. Conclusions

This paper studied the aeropropulsive interactions resulting from EDF arrays mounted at several positions along a wing to discern key insights that can be used to guide fan placement for a DEP vehicle. Twenty configurations were tested, including a Bare Wing to provide baseline aerodynamics, along with fans placed at the LE Top, TE Top, LE Centered, TE Centered, LE Bottom, and TE Bottom positions. An array of one, three, and five EDFs was tested at

each fan placement position to characterize the aeropropulsive extrapolation effects. For each fan placement and array size configuration, several angle-of-attack and throttle sweeps were performed to understand the dependence of the aeropropulsive effects across these factors. In addition to wind-on sweeps, wind-off sweeps were also performed to characterize the static propulsive array effects on total thrust, normal force, and pitching moment.

Several research questions were posed, and the aeropropulsive effects were studied for C_N, C_X, and C_m, with key insights extracted through data comparison and analysis. Across the fan positions, the C_N results showed how DEP may be used for augmented lift or roll control, the C_X data demonstrated the fan effectiveness for thrust and yaw control, and the C_m data revealed the DEP effect on static stability and pitch control. The relative suitability of each fan configuration for these various considerations was summarized, and recommendations were offered for fan placement.

The aeropropulsive extrapolation effects for the aerodynamic coefficients across each fan position were also analyzed to consider if a $1F$ experiment may be used to predict the interaction effects for DEP arrays and/or if the interaction effects from $3F$ and $5F$ configurations can be used to predict the effects from larger arrays.

The DEP research pursued in this work was enabled by the ADEPT Wing, which is a versatile capability to develop a testbed using rapid prototyping techniques for the study of aeropropulsive and propulsor-propulsor interactions. Through a combination of COTS components, 3-D printing techniques, and waterjet aluminum parts, the wing was developed with cost-effective approaches and in a reconfigurable manner for a variety of fan integration approaches. The same process may be used for similar applications that study alternative propulsors and wing designs.

The fan position results and recommendations summarized in this paper are based upon the longitudinal aeropropulsive interactions for the ADEPT wing tested in subsonic, incompressible flow conditions with uniform fan speed commands across the array. They do not include other considerations that must be accounted for in a more general vehicle design, such as wingtip effects, transonic effects, full-vehicle aeropropulsive interactions, structural integration, cost, manufacturability, and acoustics. As a result, these insights are meant to inform only part of the total cost function for DEP integration decisions.

Acknowledgments

This work was supported by the NASA Convergent Aeronautics Solutions (CAS) project SUbsonic Single Aft eNgine (SUSAN) activity. The efforts and contributions of several individuals are gratefully acknowledged for participating in the development and execution of these experiments, including David North, Ronald Busan, Wes O'Neal, Earl Harris, Rick Thorpe, Clinton Duncan, Lee Pollard, Mario Smith, Eli Etheridge, John Inge, Garry Qualls, Andrew Peterson, and Lawrence Taylor. The Larkworks MakerSpace also contributed substantially to the ADEPT Wing manufacturing.

The use of trademarks or names of manufacturers in this report is for accurate reporting and does not constitute an official endorsement, either expressed or implied, of such products or manufacturers by the National Aeronautics and

Space Administration.

References

[1] "NASA's Electrified Aircraft Propulsion Research and Development Efforts," NASA Office of Inspector General, IG-23-014, May 2023. URL https://oig.nasa.gov/wp-content/uploads/2023/12/ig-23-014.pdf.

[2] Kim, H. D., Perry, A. T., and Ansell, P. J., "Progress in Distributed Electric Propulsion Vehicles and Technologies," NASA Report Number AFRC-E-DAA-TN76298, 2020. URL https://ntrs.nasa.gov/api/citations/20200011461/downloads/20200011461.pdf.

[3] Hermetz, J., Ridel, M., and Döll, C., "Distributed Electric Propulsion for Small Business Aircraft - A Concept-Plane for Key-Technologies Investigations," *30th Congress of the International Council of the Aeronautical Sciences (ICAS)*, September 2016.

[4] Maliska, H., Schultz, V., Clarke, S., Borer, N., and Schlickenmaier, H., "X-57 Maxwell Lessons Learned Report," NASA Report Number LL-CEPT-025, 2024. URL https://ntrs.nasa.gov/api/citations/20250001718/downloads/X57%20LL%20%20public_Signed.pdf.

[5] Schiltgen, B. T., and Freeman, J. L., "ECO-150-300 Design and Performance: A Tube-and-Wing Distributed Electric Propulsion Airliner," *AIAA SciTech 2019 Forum,* AIAA Paper 2019-1808, January 2019. https://doi.org/10.2514/6.2019-1808.

[6] Goldberg, C., Nalianda, D., Pilidis, P., and Singh, R., "Economic Viability Assessment of NASA's Blended Wing Body N3-X Aircraft," *53rd AIAA/SAE/ASEE Joint Propulsion Conference,* AIAA Paper 2017-4604, July 2017. https://doi.org/10.2514/6.2017-4604.

[7] Couluris, G. J., Signor, D., and Phillips, J., "Cruise-Efficient Short Takeoff and Landing (CESTOL): Potential Impact on Air Traffic Operations," NASA/CR-2010-216392, October 2010.

[8] Schmollgruber, P., Donjat, D., Ridel, M., Cafarelli, I., Atinault, O., Francois, C., and Paluch, B., "Multidisciplinary Design and performance of the ONERA Hybrid Electric Distributed Propulsion concept (DRAGON)," *AIAA SciTech 2020 Forum,* AIAA Paper 2020-0501, January 2020. https://doi.org/10.2514/6.2020-0501.

[9] Perry, A. T., Ansell, P. J., and Kerho, M. F., "Aero-Propulsive and Propulsor Cross-Coupling Effects on a Distributed Propulsion System," *Journal of Aircraft*, Vol. 55, No. 6, 2018, pp. 2414–2426. https://doi.org/10.2514/1.C034861.

[10] Perry, A. T., Bretl, T., and Ansell, P. J., "Aeropropulsive Coupling Effects on a General-Aviation Aircraft with Distributed Electric Propulsion," *Journal of Aircraft*, Vol. 58, No. 6, 2021, pp. 1351–1363. https://doi.org/10.2514/1.C036048.

[11] Safieh, D. A., and Rauleder, J., "Aero-Propulsive Coupling on Wing Integrated Electric Ducted Fan Systems," *AIAA SciTech 2024 Forum,* AIAA Paper 2024-1726, January 2024. https://doi.org/10.2514/6.2024-1726.

[12] Safieh, D. A., and Rauleder, J., "Effects of Aero-Propulsive Coupling on High Solidity Electric Ducted Fan Performance for Various Wing Integrations," *49th European Rotorcraft Forum*, 2022.

[13] Kerho, M. F., "Aero-Propulsive Coupling of an Embedded, Distributed Propulsion System," *AIAA Aviation 2015 Forum,* AIAA Paper 2015-3162, June 2015. https://doi.org/10.2514/6.2015-3162.

[14] Jedamski, D., Ahuja, V., Alvarez, E. J., Lakshminarayan, V. K., and Moore, M., "Distributed Electric Propulsion and Vehicle Integration with Ducted Fans," *AIAA Aviation 2023 Forum,* AIAA Paper 2023-3455, June 2023. https://doi.org/10.2514/6.2023-3455.

[15] Perry, A. T., Bretl, T., and Ansell, P. J., "System Identification of a Subscale Distributed Electric Propulsion Aircraft," *Journal of Aircraft*, Vol. 60, No. 3, 2023, pp. 702–715. https://doi.org/10.2514/1.C036616.

[16] Weinstein, R., and Simmons, B. M., "Experimental Characterization of an Electric Ducted Fan for the SUSAN 25% Scale Research Vehicle," *AIAA SciTech 2024 Forum,* AIAA Paper 2024-1524, Januray 2024. https://doi.org/10.2514/6.2024-1524.

[17] Jansen, R. H., Kiris, C. C., Chau, T., Machado, L. M., Duensing, J. C., Mirhashemi, A., Chapman, J., French, B. D., Miller, L., Litt, J. S., and Denham, C. L., "Subsonic Single Aft Engine (SUSAN) Transport Aircraft Concept and Trade Space Exploration," *AIAA SciTech 2022 Forum,* AIAA Paper 2022-2179, January 2022. https://doi.org/10.2514/6.2022-2179.

[18] Jansen, R. H., Kiris, C. C., Chau, T., Machado, L. G., Dever, T., Litt, J. S., Arthur, J. J., Lynde, M. N., Chapman, J. W., Kratz, J. L., and Turner, M. G., "Update on SUbsonic Single Aft eNgine (SUSAN) Electrofan Trade Space Exploration," *33rd Congress of the International Council of the Aeronautical Sciences (ICAS)*, September 2022.

[19] Miller, L., "Development of Subsonic Single Aft Engine (SUSAN) Attritable Research Vehicle (SARV) Wing Structure," *AIAA SciTech 2024 Forum,* AIAA Paper 2024-1523, Januray 2024. https://doi.org/10.2514/6.2024-1523.

[20] Simmons, B. M., Gresham, J. L., and Woolsey, C. A., "Aero-Propulsive Modeling for Propeller Aircraft Using Flight Data," *Journal of Aircraft*, Vol. 60, No. 1, 2023, pp. 81–96. https://doi.org/10.2514/1.C036773.

[21] Finck, R. D., "USAF Stability and Control DATCOM," AFWAL-TR-83-3048, Apr. 1978.

[22] Hall, D. K., Huang, A. C., Uranga, A., Greitzer, E. M., Drela, M., and Sato, S., "Boundary Layer Ingestion Propulsion Benefit for Transport Aircraft," *Journal of Propulsion and Power*, Vol. 33, No. 5, 2017, pp. 1118–1129. https://doi.org/10.2514/1.B36321.